2D AND 3D MAPPING OF A LITTORAL ZONE WITH UAS AND

STRUCTURE FROM MOTION PHOTOGRAMMETRY
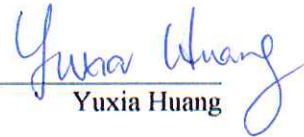
by

JUSTIN ZACHARY GIESSEL

Major Professor: _____

Michael J. Starek

Committee: _____

Yuxia Huang

_____

Richard Smith

Electronic Version Approved:

JoAnn Canales
Dean of the College of Graduate Studies
Texas A&M University – Corpus Christi
May 2015

2D AND 3D MAPPING OF A LITTORAL ZONE WITH UAS AND
STRUCTURE FROM MOTION PHOTOGRAMMETRY

by

JUSTIN ZACHARY GIESSEL

(Under the Direction of Dr. Michael J. Starek)

ABSTRACT

Advancements in the miniaturization of sensors and their integration in light-weight, small-scale unmanned aerial systems (UAS) have resulted in an explosion of uses for inexpensive and easily obtained remotely sensed data. This study examines the capabilities of a small-scale UAS equipped with a consumer grade RGB camera for 2D and 3D mapping of a sandy bay shoreline using Structure from Motion (SfM) photogrammetry. Several key components are analyzed in order to assess the utility of UAS-based SfM photogrammetry for beach and boundary surveying of the littoral zone. First, the accuracy of the 3D point cloud produced by the SfM densification process over the beach is compared to high accuracy RTK GPS transects. Results show a mean agreement of approximately 7.9 cm over the sub-aerial beach with increased error in shallow water. Minimal effects of beach slope on vertical accuracy were observed. Secondly, bathymetric measurements extracted from the UAS/SfM point cloud are examined, and an optical inversion approach is implemented where the SfM method fails. Results show that a hybrid elevation model of the beach and littoral zone consisting of automatic SfM products, post-processed SfM products, and optical inversion provide the most accurate results when mapping over turbid water. Finally, SfM-derived shoreline elevation contour (boundary) is compared to a shoreline elevation contour derived using the currently accepted RTK GPS method for conducting legal littoral boundary surveys in the state of Texas. Results show mean planimetric offsets < 25 cm demonstrating the potential of UAS-based SfM photogrammetry for conducting littoral boundary surveys along non-occluded, sandy shorelines.

INDEX WORDS: UAS, Structure from Motion, shoreline mapping, littoral zone

2D AND 3D MAPPING OF A LITTORAL ZONE WITH UAS AND

STRUCTURE FROM MOTION PHOTOGRAMMETRY

by

JUSTIN ZACHARY GIESSEL

B.S., TAMUCC, 2008

A Thesis Submitted to the Graduate Faculty of the Texas A&M University – Corpus Christi in Partial

Fulfillment of the Requirements for the Degree

MASTER OF GEOSPATIAL SURVEY ENGINEERING

CORPUS CHRISTI, TEXAS

2015

2D AND 3D MAPPING OF A LITTORAL ZONE WITH UAS AND

STRUCTURE FROM MOTION PHOTOGRAMMETRY

by

JUSTIN ZACHARY GIESSEL

Major Professor:	Michael J. Starek	
Committee:	Yuxia Huang	
	Richard Smith	

Electronic Version Approved:

JoAnn Canales
Dean of the College of Graduate Studies
Texas A&M University – Corpus Christi
May 2015

TABLE OF CONTENTS

LIST OF TABLES

LIST OF FIGURES

INTRODUCTION

1.1 Overview

Methods of remote sensing are emerging that deliver hyper-resolution aerial photography that can be processed using Structure from Motion (SfM) photogrammetric methods to produce high-accuracy, dense point clouds, digital surface models (DSMs) and orthophotos. Unmanned aerial systems (UAS) are more frequently being used as a platform for high-resolution photography because they are cheap to manufacture and operate. SfM algorithms are easily implemented into user-friendly software that requires minimal training and expertise; however, ensuring high geospatial accuracy of derived products and characterizing uncertainty can be non-trivial. This study tested the utility of using Structure from Motion (SfM) photogrammetry to map littoral boundaries using imagery acquired by a small-scale, light-weight unmanned aerial system (UAS). Modern small-scale and electric powered fixed-wing UAS equipped with a high resolution (>12 megapixels) digital camera are capable of autonomously capturing high resolution imagery over several square kilometers (ex. 12 km^2) on a single flight though the total area covered will depend on battery endurance, flying height, wind, and other factors (Sensefly, 2014). Ground sample distance (GSD), or resolution on the ground, for imagery captured by low altitude (<130 meters) aerial photography is typically centimeter or an order of magnitude higher. Advances in navigational sensors and inertial measurement units (IMU) have led to the development of micro-electronic mechanical systems (MEMS) which comprise the miniaturized 3-axes accelerometers, rate-gyros, and electronic compasses (Jiang et al., 2012; Ma et al., 2012). The components coupled with onboard GPS all provide real-time data enabling autonomous flight, and providing attitude and georeferencing data for simultaneous storage with imagery. Miniature electronics and high resolution consumer digital cameras are merged in the UAS to provide an ultra-light and portable means to collect remotely sensed data. Automatically executed flight plans including the triggering of the camera shutter enables the user to quickly mobilize the UAS and collect imagery. From this imagery it is possible to

produce 3-dimensional point clouds and digital elevation model (DEM) as well as orthophotos via the SfM pipeline.

SfM is a computer vision-based workflow in which sets of high resolution overlapping images can be processed in order to solve for camera orientation and pixel coordinates in real coordinate space by using image-to-image registration methods called feature detection and correlation. Images from non-metric cameras are suitable for processing using a SfM approach, which gives this workflow a distinct advantage over traditional photogrammetric routines (Mancini et al., 2013). The calculated relationships are used to create 3-dimensional models that are subsequently used to orthorectify the imagery and create orthomosaics with color attributes. SfM utilizes techniques in digital image processing to identify and track patterns of pixels, or features, in multiple images. Using autonomous GPS positions and inertial measurement unit (IMU) data for initial camera orientation values, a system of highly over-determined equations can be produced using constraints imposed by matched features and camera model attributes. Final processing involves determining interior and exterior camera orientation as well as the position of each common pixel identified in overlapping photos (densification). The final products are typically a 3-dimensional point cloud, digital surface model (DSM), and orthomosaic.

<div align="center">1.2 Motivation</div>

The littoral boundary is the complex interface between the sea and land; it typically refers to a beach system with shoreline and a fluctuating tidal level that exposes or covers part of the beach. Various water levels, represented by contours, are of legal importance in the United States because they often times represent a cadastral boundary or the limit of jurisdiction for a governmental agency. For example, in Texas, Spanish and Mexican law govern that the upper limit of public land from the sea as "all that place [which] is called shore of the sea insomuch as it is covered by the water of the latter, however most it grows in all the year, be it in time of winter or of summer…" as defined in 'Las Sietes Partidas' or the Seven Parts Code - laws from the monarchy of 13th century Spain (McFarland, 2013). In the Texas Supreme Court case Luttes versus State of Texas, it was decided that a scientific approach would be used to determine this location, and would be defined as "the line of mean higher high tide

(MHHW). The use of a tide gauge would be used for determining boundary locations in Texas. One of the primary goals of this research was to experiment with remotely sensed data captured using a portable and inexpensive UAS for mapping specific contours such as MHHW. MHHW contours are currently found in the field using traditional leveling techniques, total station, or more recently with GNSS observations.

UAS are providing a suitable vehicle by which low-altitude spectral data can be obtained, but the use of UAS in the United States is currently restricted. According to the Federal Aviation Administration (FAA) website, civil operations of UAS are limited to research and development, crew training, and market surveys. Aircraft require an airworthiness certificate (FAA, 2015). Carrying persons or property for compensation or hire is currently prohibited, which effectively blocks most organizations from pursuing UAS utilization in the United States. Despite impeding regulation on UAS usage in the United States, proposed rules providing for the integration of UAS into the U.S. airspace were released February 15, 2015. Highlights from FAA proposed rules include a maximum flying altitude of 500ft, a maximum weight of 55 pounds, the passing of aeronautical knowledge exam by operators, and the exclusion of an airworthiness certificate. Commercial operations under these proposed rules are on the horizon. Current UAS use in the United States under 'public/governmental' use and sanctioned civil operation include law enforcement, search and rescue, forensic photography, border security, weather research, and scientific data collection. The potential for commercial use is virtually unlimited, but includes activities such as land surveying, pipeline/utility right of way mapping, agricultural/farm inspections, vehicular traffic monitoring; real-estate and construction-site photography, telecommunication signals relaying, film industry production, fishery protection and monitoring, and many other geological/environmental monitoring activities. Forecasts for the eventual growth of UAS industry expect growth exceeding $89 billion over the next decade (USGOA, 2015).

UAS-derived data could potentially be utilized to map littoral boundaries for taxation purposes or for planning and decision-making purposes regarding expanses of inaccessible land. In Italy, Mancini et al., (2013) have used UAS and SfM combinations have been shown to be effective in high resolution

monitoring of beach and dune systems with an average vertical residual between SfM point clouds and terrestrial laser scanning (TLS) point clouds of approximately 5 centimeters (cm). Accurate and inexpensive mapping of the littoral zone along the Texas coast has implications in land management, erosion protection/prevention, and habitat or environmental monitoring. UAS photogrammetry could provide for a cost-effective method to obtain accurate elevation and spectral data in areas difficult to access such as deltaic marshes, remote beaches, and islands. The technology and workflow presented here offer an alternative to field intensive GNSS and TLS surveys, or expensive airborne lidar coverage. GNSS surveys currently utilized for monitoring purposes are cost-prohibitive, and UAS-derived spatial data may provide a means to survey areas where available budget cannot provide for base and rover survey. For example, recent communications with Texas General Land Office (Pers. Comm. TXGLO Survey Div.) indicate that the survey division would be interested in implementing a UAS-derived photogrammetry workflow that could produce an accurate elevation model and orthomosaic. Usage discussed included the delineation and quantification of artificial fill/buildup as part of the requirements for state-funded erosion protection programs (Texas Administrative Code 33.136).

The utility of 3-dimensional SfM data was examined by applying it to a survey environment along a littoral zone where a portion of the scene was underwater. For this study, the effectiveness and accuracy of image-matching and modeling along a sandy, low gradient beach, and through shallow, turbid water was assessed and quantified. Accuracy was assessed by comparing SfM point cloud data and planimetric location of SfM-derived MHHW contour to GNSS survey data. It was hypothesized that SfM would fail over portions of the water surface where turbid water inhibits feature matching and correlation from the seafloor and effects of the dynamic water surface, specular reflection, and changes in view and lighting conditions from image to image impose a quasi-random element that cannot be appropriately matched and tracked between correlated photos. Results show that with careful survey design and post-processing, reliable information can be extracted from the sub-aerial beach and submerged zone to derive accurate shoreline boundaries and elevation models.

The study is outlined as follows. First, a side by side comparison is made between 3-dimensional point cloud measurements derived from UAS acquired imagery using SfM photogrammetry and in-situ RTK GPS survey data. Next, a method of band ratio optimization, or optical (bathymetric) inversion, is tested for use in obtaining bathymetric data from 3-band RGB imagery where the water surface occludes and disrupts the SfM feature matching process. Post-processing and classification methods are implemented on the SfM derived values to fuse different model outputs and derive a seamless topo-bathymetric map. Finally, MHHW shoreline extracted from the SfM-derived digital elevation model is compared to in-situ RTK GPS shoreline observations representing the currently accepted method used in legal littoral boundary surveys. The ultimate goal of this study is to assess the appropriateness of using a SfM workflow in littoral boundary surveying, and also to identify best practices as well as potential problems with using UAS photogrammetric techniques in these environments.

Chapter 2 details background material and literature on SfM photogrammetry. Chapter 3 presents measurement methods including detailing the study area and the UAS utilized in the research. Chapter 4 presents results and a discussion on the findings. Chapter 5 provides concluding remarks, and Chapter 6 outlines future work.

CHAPTER 2

BACKGROUND

2.1 Structure from Motion

SfM refers to the workflow and set of algorithms used to determine 3-dimensional coordinates of an object space from a series of overlapping photographs (Jebara et al., 2001). Any camera or scanner measures the intensity of light at a particular location. The SfM goal is to derive 3-dimensional information from these measurements and their origins. Interior and exterior camera orientation are solved by placing geometric restraints on the images by identifying and tracking features in multiple photographs. The SfM pipeline is a combination of modules where output from one is fed into another (Graham, 2005).

Camera model:

The camera model is crucial because the SfM process is based on the theory of adjusting or solving for rays of light passively traveling from the reflective surface of the earth/object through an orifice and lens to a particular position on a CCD sensor. The camera model is the nexus for three crucial transformations (Graham, 2005):

1. A coordinate transformation relates real-world points to a position on the camera sensor
2. A projection occurs when rays being received from a 3-dimensional world intersect a 2-dimensional sensor plane.
3. Transformations between series of photographs.

Initial values for interior and exterior camera orientation during initial processing is supplemented by the information stored in exif (exchangeable image file format) data. Most modern digital cameras embed useful information about each photograph into the image file. These data contain information such as GPS location (if equipped), compass heading, exposure time, focus, aperture, and focal length. Focal length is crucial in solving the constrained equations used in the SfM pipeline (Snavely, 2008). A network of system constraints allows for the automated calculation of intrinsic camera properties for a particular project during the SfM process including the calibrated focal point, principle point, lens distortions, skewness, and pixel ratio which is why non-metric cameras are acceptable for use.

6
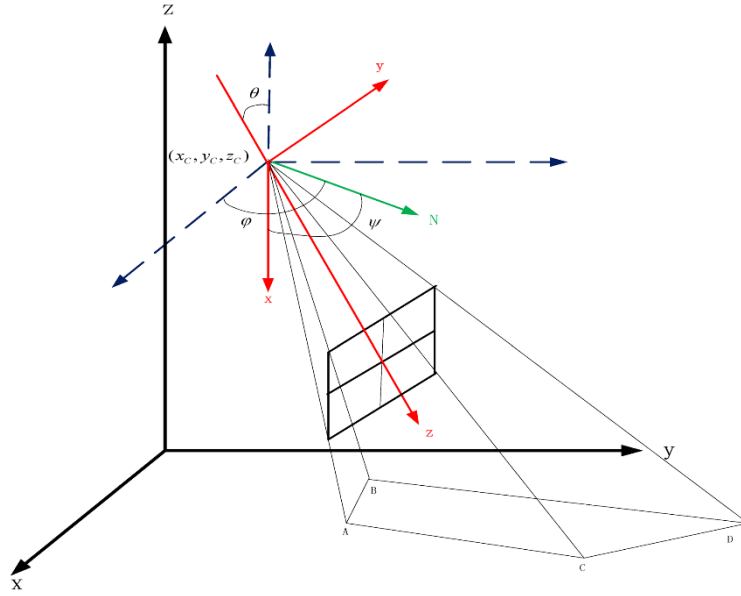
Figure 2.1: Camera Model: Field of view of a camera showing components to exterior orientation such as yaw, pitch, and roll angles (ϕ, θ, ψ) (Fu et al 2014). Also shown is a visualization of the projection from 3-dimensional real-world coordinates to the 2-dimensional coordinate plane of the camera's sensor or film.

Because no a priori knowledge is necessary in SfM, the process relies on matching multiple features in multiple overlapping images. The overdetermined system of equations and relationships eventually allows for triangulation of individual rays and the solving of camera orientations (Figure 2.1). The need for constraint in solving a highly overdetermined system translates to high image overlap when developing a dataset for use with SfM. Typical SfM flight plan recommendations call for approximately 70% sidelap and 80% frontlap of photography (Pix4D, 2015).

SfM software:

The SfM process has been automated and bundled in a variety of commercial software packages exist for SfM processing of imagery acquired from most any camera model. One of the most well-known SfM photogrammetry software suites is called Pix4D, which forms the engine behind the SfM post-processing software packaged with the UAS system used in this study (see Chapter 3 for details on the software and UAS system used in this study). Image matching and camera orientation in the Pix4D workflow are completely automated; however, the program does offer the user a variety of processing options and variable parameters. Open source SfM packages exist as individual modules to the SfM pipeline; they are mostly collections of software written by academia for doctoral thesis projects including VisualSFM: A Visual Structure from Motion System (Changchang Wu), PMVS-SfM: Patch-based Multi-

view Stereo Software-PMVS – Version 2 (Furukawa and Ponce, 2010), Sparse Bundle Adjustment

(Lourakis and Argyros), and Bundler: SfM for Unordered Image Collections (Snavely, 2006). These

tools are finding wide scale utility.

Feature Detection:

Image matching is the first problem in SfM workflows (2D correspondence problem)(Graham,

2005). SfM depends on image matching to identify and describe relationships between images. Feature

detection in subsequent photographs is what enables the SfM algorithm to constrain camera orientation

with collinearity equations. It is thus one of the most important modules in the SfM pipeline. Most

algorithms assume that features from different photos will appear similar (Snavely, 2008). A multitude of

image edge and corner detecting algorithms exist; most function by employing a moving array with

varying attributes. Examples include Harris detector, ORB, FAST, and SURF. The Harris Corner

Detector is one of the earliest feature detectors, and functions by applying a matrix computed over a

window region of an image that compares computed values within that window to a user-defined

threshold. Edges are found by identifying patterns in values within the array. If the windows exceeds the

threshold, the feature is identified as a point feature. Edges, however, are difficult to track because they

fragment differently within a series of photos and are thus untrackable (Harris and Stephens, 1988). More

recent developments in feature detection include the most popular feature detector - scale-invariant

feature transform (SIFT), that locates features in image coordinates by applying the differences between

Gaussian filters of a pair of images to find all local minima and maxima. Differences of Gaussian filters

are used to locate the image coordinate (x,y) center of patches, as well as corners where lines meet

(Snavely, 2008). Histograms are computed for local areas of each image and gradient vectors are created

for 8 directions so that higher order patterns can be identified (Teeravech, 2015). The algorithm is thus

able to recognize features regardless of scale and orientation/perspective that the image is taken so that

multiple photos from different cameras can theoretically be used to construct a model. This is a beneficial

feature for UAS acquired imagery. The SIFT algorithm excels in situations where high resolution imagery

is used that yields the most features with a more accurate point set. Regularization constraints are also

part of the image matching process, which remove transient objects such as helicopter landing skids, kite tether, tourists, etc. The use of consumer grade cameras and low-flying or hand-held photography makes possible low cost topographic surveys which are suitable in certain scenarios (Fonstad et al 2012). Instead of relying on a simple image cross-correlation, which relies heavily on a constant scale, SfM matching algorithms also rely on color gradient matching at multiple scales. These algorithms also function regardless of resolution miss-matches.

Dense matching:

Dense matching is the populating of individual pixel locations using the model properties calculated during computation of camera orientations/positions and sparse model. A theoretical ray is computed for individual pixel pairs after orientation is established. 3-dimensional location is triangulated through parallax of the image sets (Tola et al., 2010). Various methods exist for dense matching although generally all incorporate a moving window which is located in image space using the pre-established matches described in initial processing. Since camera calibration data have already been determined in initial processing, initial values for expected location of correspondence is estimated. In this manner features are found at a much higher resolution; optimally, each pixel is co-located. Computational resources are used efficiently by dense matching after initial camera orientations are computed in groups or bundles. If the moving array can identify common pixels in two photographs with orientation information then a 3-dimensional point can be extracted (Megyesi, 2009). Algorithms for dense matching include previously mentioned patch-based multi-view stereo (PMVS), semi-global matching, and MICMAC (Dall'Asta and Roncella, 2014). The methods allow for the use of stereo information in the automatic filtering of matching errors by using the sparse model as absolute reference measurements (Wohlfeil et al., 2013). The resultant point cloud can be used in the same manner as a lidar point set. For example, the point cloud can be used in a GIS for deriving digital terrain models or in a CAD environment for creating a surface and rendering profiles or volume calculations.

The orthomosaic product is produced similarly to the point cloud with the key difference being that individual pixels are projected from real coordinate space to a grid coordinate system to remove relief

distortion; pixels of a particular resolution, color, and location are projected from the 3-dimensional model on a 2-dimensional surface. Orthomosaics produced using SfM are not the result of the stitching together of imagery, but rather the projection of individual pixels from the original imagery. A DEM, or terrain mesh is used as the base surface from which pixels are projected so that oblique perspective is removed. Multiple overlapping images contribute to the final orthomosaic. The relative contribution of each photo is dependent on a defined system of weights relative to the proximity of each camera principal point to the pixel (Pix4D, 2015). The finished product is a complete orthophoto whose color properties are defined by individual pixel combination according to these weights. Transformation from arbitrary model coordinates to 3D real world coordinates is the last process in the SfM workflow. The final coordinate transformation process is described in the methods (Chapter 3).

<u>2.2 SfM Uses</u>

Researched uses of UAS SfM photogrammetry include forestry, river bed topography, river bank morphology, glaciology, rock slope stability analysis, and coastal dune system analysis. SfM has been used to map microscale topography and geology such as fault breaks and associated features. Johnson et al., (2014) demonstrate that imagery captured from low altitudes between 50 and 60 m can be used in SfM to produce DEMs of fault zones with reported average vertical residuals less than 6 cm when compared to TLS, and point cloud densities between 530 points/meter^2 and 700 points/meter^2. Similar research by Vasuki et al., (2014) compares SfM results to manual digital image interpretation of 3-dimensional orientations of mapped geological structures. Slopes derived from SfM models showed a mean standard error of 1.9° +/- 2.2° and 4.4° +/- 2.6°. Another geological use of UAS SfM modeling is the monitoring of micro-scale landslides in southern Tasmania where an octo-rotor UAS was used to acquire aerial photography at 1 cm resolution. A horizontal RMSE of 7.4 cm and vertical RMSE of 6.2 cm was reported. Features such as scarps, toes, and patches of vegetation were tracked and semi-automatically mapped using an image matching algorithm (Lucieer et al., 2013).

2.3 SfM versus Softcopy Photogrammetry

The basic concept of all methods of aerial photogrammetry is the correlation of two-dimensional coordinates from a developed camera film (or digital equivalent) to 3-dimensional object space coordinates by solving for collinearity equations (describing the orientation of the camera, camera model, and individual ray) (Wolf et al., 2014). Exterior orientation is the determination of camera location and direction in 3-dimensional space by solving collinearity equations using known ground control points or from the measured coordinates and orientation of the camera focal point. Traditional softcopy photogrammetry requires knowledge of initial orientation of camera position or location of 3-dimensional control within the project. If 3-dimensional point locations are known in real coordinates (or fudicial marker locations) the position of the camera can be backsolved via a process called space resection (Snavely, 2008). In softcopy photogrammetry, point densification is accomplished via moving window techniques, which are used to match image features and locate pairs of two dimensional image coordinates from stereo pair photos in 3-dimensional space via triangulation (Woodget et al., 2014). Instead of traditional feature collection practices, developments in computer vision software have enabled the use of automatic image matching, which can simultaneously and systematically scan photographs in a stereo pair and match individual pixels (Linder, 2009). Recent image matching algorithms assess the quality of the matched pixels and assign them an ordinal value based on the quality of the surrounding pixel's correlation. Areas with non-matches are interpolated using neighboring values (Westaway, 2009). The process seeks to minimize a geometric cost function by jointly optimizing both the camera and point parameters using non-linear least squares (Snavely, 2008). According to Butler et al., (1998) (from Westaway, 2009), the quality of the DSM created using photogrammetric methods is directly dependent on how well the collinearity equations describe the relationship between derived coordinate values and actual object space coordinates. The critical divergence from traditional photogrammetry is that the SfM algorithm is suited for matching photographs taken from random locations assuming that coverage of a surface is present in at least two photographs (Snavely et al., 2009). Progresses in image matching like the SIFT algorithm enables the use of imagery from a wide range of perspectives. These approaches

contrast from traditional airborne photogrammetry, which assumes parallel flight lines with overlapping photos and expensive well-calibrated metric cameras (Fonstad et al., 2012).

Image matching is the technology that drives softcopy photogrammetry and recent progresses in this field are the core of SfM. SfM is a set of iterative algorithm pipelines that can solve simultaneously both unknowns with no a priori knowledge of either. Bundle adjustment is the term used to describe the solving of collinearity equations for multiple pixels simultaneously. Traditional photogrammetry requires that the position and orientation of the camera be precisely known and/or as well as ground control points (resectioning). Triangulation can be used in conjunction with 3D control points when camera orientation is unknown. On the other hand, SfM photogrammetry systematically solves for camera position as well as interior and exterior camera orientation via bundle adjustment based on feature matching from a series of overlapping photos and requires neither camera orientation nor 3D control points (Westoby, 2012). Features are tracked through various overlapping photos and initial estimates of interior/exterior orientation are refined using least squares. One advantage of using a SfM approach to produce final models include the suitability of images from non-metric cameras for processing.

Another crucial difference between SfM and traditional photogrammetry is that collinearity equations are solved using image matches before introducing a transformation using GCPs. Models (point clouds) are created independently of the real coordinate space 3-dimensional control. The model is later transformed from an arbitrary coordinate system based on photo coordinates to the coordinate system of introduced ground control. Similar to traditional photogrammetry, a minimum of three ground control points with known XYZ coordinates must be identified in each stereo pair, or the six camera parameters at the time of each photograph exposure (XYZ position of camera principal point and attitude or three rotation angles). The drawback is that inaccuracies introduced during the conjugate pair matching before GCP transformation can introduce uncorrectable errors that propagate when the model is located using real world ground control. The other disadvantage is that the transformations are purely linear and non-linear introduction of error such as lens distortion cannot be removed (Fonstad et al., 2012). Ground control must be located within the project site and visible on multiple images from the

acquired photography in order for georeferencing of the post-processed images and subsequent models (Woodget et al., 2014). Two solutions exist to tie the SfM point cloud to a ground coordinate reference system; the classical rigid 7-parameters Helmert transformation and the bundle adjustment procedure (Mancini, 2013).

<div align="center">2.4 SfM versus Lidar</div>

The most comprehensive alternative to photogrammetry for 3D imaging and elevation modeling is airborne light detecting and ranging (lidar). A lidar point set can contain millions of laser returns that are ranged using time of flight measurement of the returned backscattered laser pulse. Lidar does produce near 100% coverage, unlike typical GNSS surveys, which are primarily sampled along transects. Lidar missions, however, are extremely costly, requiring an airplane to carry the equipment payload. Additionally, the final point set does not match the vertical accuracy of a survey-grade GNSS survey or total station topographic survey. Terrestrial Laser Scanning (TLS) is the terrestrial version of airborne lidar by mounting a lidar scanner on a static tripod and typically operates by emitting and receiving an oscillating pulse from a rotating head giving the instrument 360 degrees of view. TLS has been used along coastal areas to produce DEMs with vertical accuracies of 3 cm or better (Mancini, 2013). Much research has been done comparing results from these three survey methods (Skarlatos and Kiparissi, 2012; Beraldin et al, 2004). For the most part, research shows that under ideal conditions (little vegetation, low flying altitude), SfM derived UAS products are comparable to TLS or airborne lidar. Lidar/TLS have become the standard for production of dense point clouds because of the accuracy and automation built into these systems. Furthermore, airborne lidar systems provide multi-return capabilities enabling measurement below vegetation canopy. Photogrammetry is a single return system meaning we get one potential 3D measurement per an overlapped pixel. In cases where measurement of bare-earth surface occluded by vegetation is desired, lidar is the clear winner.

It has been predicted that scanning may completely replace photogrammetry practices in the near future (Boehler and Marbs, 2004). However, both the remote sensing and computer vision community

<div align="center">13</div>

have taken a renewed interest in automated image matching and feature tracking using cameras. Advances in these fields have led to the development of inexpensive methods to collect and process spectral data as well as produce high resolution point clouds comparable to laser scanning at a fraction of the cost (e.g. $150 handheld digital camera vs $100,000 laser scanner). The biggest drawbacks of laser scanning still include the high cost of equipment, portability, time consuming data acquisition, noise from non-target objects, and low quality color information (Skarlatos and Kiparissi, 2012). Comparisons of the two technologies suggest that instead of being in competition, laser scanning and photogrammetry may be complementary technologies. For example, the Pix4D software is capable of processing datasets from any scale level as long as the entire dataset is captured at a similar scale (i.e. Pix4D can be used in micro-scale terrestrial reconstruction of a single building or used with satellite imagery for reconstruction of a mountain). A single SfM package has the ability to automatically solve for camera orientations and scale based on control points. Conversely, laser scanning demands suitable equipment for multiple scale levels (i.e. airborne lidar system versus various TLS equipment). Experiments show that SfM outperforms TLS in some aspects under certain condition such as the better preservation of texture while still producing an equally dense and accurate point cloud (Skarlatos and Kiparissi, 2012). Stockpile volume analysis using Pix4D and Sensefly Swinglet UAS have produced volumes comparable to volumes calculated using GNSS survey methods. In fact, Draeyer and Strecha (2014) show that bare stockpile surfaces can be located to within 3X ground sample distance (GSD). In the case presented, 95% of surface locations between GPS and Pix4D SfM varied by approximately 15 cm or 3X the 5 cm GSD. Another advantage of SfM is that data is sampled at approximately equal ground sampling distance unlike TLS which samples at a denser rate near the scanner and becomes sparser as distance increases.

Lidar is a proven technology, though some of the same problems are encountered in an aqueous medium such as the refraction of light through the air-water interface. However, blue-green wavelength (532 nm) bathymetric airborne lidar systems such as the Optech Aquarius and Leica AHAB Chiroptera are capable of successfully penetrating the water column of up to 12 m and 10 m, respectively dependent on clarity. Higher energy bathymetric lidar systems, such as USACE's CZMIL, can penetrate to depths of

30 to 40 meters or greater in clear water. Bathymetric lidar accuracies depend on the refraction correction and bottom surface reflectivity as well as sensor characteristics among other factors. For example, the reported vertical RMSE of an airborne bathymetric lidar survey of a shallow water bay in Aransas Pass, Texas conducted using the Optech Aquarius system was 0.175 m (Fernandez-Diaz et al., 2014).

<u>2.5 Challenges along the Beach</u>

SfM approaches are appealing for modeling vast expanses of terrain quickly and efficiently. Application of UAS imagery and SfM modeling in support of coastal projects includes 2D (horizontal) positioning of features such as contour lines as well as production of 3D terrain models along the shoreline. The challenges of using visible light for remote sensing around shorelines include the occlusion of ground points by vegetation and rapid attenuation of light through the water column where present if desiring to map the bathymetry. In a bathymetric setting, addition obstacles to accurate modeling are encountered such as the refraction of light propagating across mediums and the unintentional modeling of the water's surface when sufficient disruption (surface waves/white water) are present during survey. Westaway et al., (2001) showed that digital photogrammetric derivation of DEMs can be achieved for submerged topography within a clear water, shallow, gravel-bed river system of New Zealand. Westaway implements a corrective regression for refraction of light through the clear water column. The research reports a mean error of 0.188 m for corrected depths realized via SfM photogrammetry. Research along a sandy shoreline by Mancini et al., (2013) showed that although the majority of elevations extracted using SfM photogrammetry were comparable in accuracy to GNSS solutions, the method is prone to failure along flat portions of beach where the surface is very homogenous. Smooth surfaces are difficult for pixel by pixel image matching, and can result in a less dense point cloud.

Refraction of visible light through water:

The refraction of light occurs when light passes through mediums of different physical properties. The change in direction of the entering and returning light waves complicates bathymetric

15

photogrammetry. Effects of refraction generally cause the subsequent models to overestimate elevation (underestimate water depth). Water depths less than 0.2 meters show negligible degradation from refraction (Woodget et al., 2013).

These basic laws are described by Snell's laws:

$$\sin i = n \sin r$$
$$r = \arcsin((\sin i)/n)$$

where i = angle of incident of the light ray above the water's surface; r is angle of refracted ray below the water's surface; and n = the refractive index for both the mediums. This refractive index, n is equal to approximately 1.34 in clear water. Fernandez-Diaz et al., (2014) use a refractive index of 1.333 for lidar measurements across Redfish Bay near Aransas, Texas. Methods have been established to adjust rays that pass through water by applying a refraction correction procedure (Westaway et al., 2000). The method involves mapping and modeling the surface of the water by extracting elevations along the edge of the water and interpolating the whole water surface. Two other models are created for the subaqueous bottom: a non-corrected determination and a corrected model using an appropriate refractive index. By finding the difference between the corrected and uncorrected bathymetric models and subtracting that difference from the water surface triangulated irregular network (TIN), depths can be calculated for points through the water. Westaway concludes that correctly solving collinearity equations given the refraction of light between two mediums is the key to more accurate bathymetric photogrammetry. Since average water depth for the university beach project area was 42.7 cm (1.4 ft) and 77.4 cm (2.5 ft) for August 24 and October 5, the errors introduced as a result of refraction were ignored.

2.6 GNSS Surveying

In the late 21st century the Real Time Kinematic (RTK) GPS has become the survey standard for measuring horizontal and vertical positions. Analysis of SfM products in this research effort were directly compared to GNSS observations based on RTK corrections from Trimble's VRS network. Corrections are transmitted over the internet and received via GSM cellular phone connection.

Conventional GPS topography surveys are field intensive and can be difficult in terrain where substrate is soft or access impeded by water, mud, etc. Most topographic surveys extending into an area covered in water are conducted using GNSS with RTK corrections via range poles and a technician. The US Army Corps of Engineers hydrographic survey manual specifies that most shoreline topographic surveys can be performed using an established baseline with stationing perpendicular to grade (USACE, 2013). RTK GPS surveys are intensive, and require field personnel, equipment, and time. Bathymetric RTK surveys are effective, but rely on range rods that can be extended to the intended depth to be surveyed. At greater depths, acoustic hydrographic methods are commonly used including single beam and multibeam sonar. All of these survey techniques require a great amount of equipment as well as field personnel. The data must also undergo post processing techniques. Bathymetric data must be adjusted for variable speed of sound in water. Another weakness is that all modeling between stationing will be primarily interpolated unless a grid or other survey sampling setup is utilized. Both of these modifications add to the time and cost of the survey. GNSS-based survey methods are time and cost intensive, and the ultimate goal of utilizing UASs and advanced SfM algorithms for photogrammetric derivation of DSMs is to replace or supplement traditional methods for certain types of surveys. Positional accuracies for typical differentially corrected RTK are 1cm + 1ppm horizontal and 2cm +1ppm vertical. Photogrammetric methods of obtaining DSMs have the potential to minimize some of the time and expense that might otherwise be spent on conducting a standard topographic survey using GPS or total station methods; however, the achievable accuracy is generally lower (Westaway, 2001).

2.7 Optical Inversion

It was hypothesized that supplemental sub-surface point elevation data might be extracted from the georeferenced orthomosaic reflectance map output from SfM using an optical inversion approach based on a specific band ratio. Optical inversion calculations for depth were tested using the obtained spectral imagery and optimized band ratio analysis (OBRA) method (Legleiter, 2011). OBRA methodology involves the comparison of the natural logarithm of a ratio of recorded wavelengths of light

to known depth values in order to find the optimal ratio for measuring depth (Eq. 1). Previous works use a regression matrix to calculate the most probable relationship of the ratio compared to in-situ observed depths as follows:

$$\text{Depth} = m_o \frac{\ln(R\lambda 1)}{\ln(R\lambda 2)} + m_1 \ \ (\text{Eq. 1})$$

where R = reflectance measured in two spectral frequencies centered at wavelengths λ_1 and λ_2, and λ_2 = max; m_o and m_1 are regression constants that have to be derived using in-situ observations.

Both Legleiter (2011) and Pan et al., (2014) found a particular yellow wavelength over red wavelength - 591nm/648nm and 585.9nm/633.6nm respectively to be the optimal wavelength ratio for deriving a depth/reflectance relationship. Several combinations of smoothed bands $\log(\text{band}_1)/\log(\text{band}_2)$ were used in order to derive some depth information from IXUS Canon camera band reflectance values. Since the water in along the Texas coast is so turbid, other methods of deriving depths from spectral imagery including image matching coupled with refraction corrections are not being considered in this study.

CHAPTER 3

RESEARCH METHODOLOGIES AND CONCEPTS

3.1 Study Area and Survey Methods

The study area was the university beach at Texas A&M University Corpus Christi (TAMUCC)(Figure 3.0). University beach lies adjacent to the TAMUCC campus on the south shore of Corpus Christi Bay on Ward Island where previous shoreline existed before the occupation of the Encinal Peninsula. The original shoreline was lost, and the beach today was constructed in 2001 from imported materials (Williams, 2002). The beach is actively monitored by the Conrad Blucher Institute. Topography from south to north features the slope and toe of Ocean Drive (an improved 4-lane paved road), a gently sloping sand beach, shoreline, seafloor with sand bottom and seagrass bottom, as well as two rock jetties and three breakwaters.

GNSS Survey

The objective of this research was to quantify the accuracy of various SfM products including point cloud data and isolines derived from SfM elevation data as well as a DEM created by optical inversion. These products and combinations of these products were compared to an RTK GPS topography survey. GPS observations were recorded along parallel transects on August 22, 2014. Transects ran perpendicular to Ocean Drive, and were spaced 30.48m (100 ft) apart; some transects on the peripheral edges of the study zone were spaced 45.72m (150 ft) (Figure 3.1). This network of RTK GPS observations served as control for analysis of remotely sensed data (SfM point cloud and optical inversion DEM). GPS observations were tied to a National Geodetic Survey (NGS) benchmark that was checked against an OPUS solution (PID: AC8481, Designation: B010). GPS observations were recorded using RTK corrections from Western Data Systems' VRS network. Coordinates were stored in North American Datum of 1983 (NAD83), Texas State Plane South Zone, and elevations were recorded in North American Vertical Datum of 1988 (NAVD88). Spacing between GPS observations along transects varied in order to capture all present topography within the project area. On average, GPS observations were spaced approximately 1.45m (4.75ft) (1,365 GPS points/6480 ft total transect length).
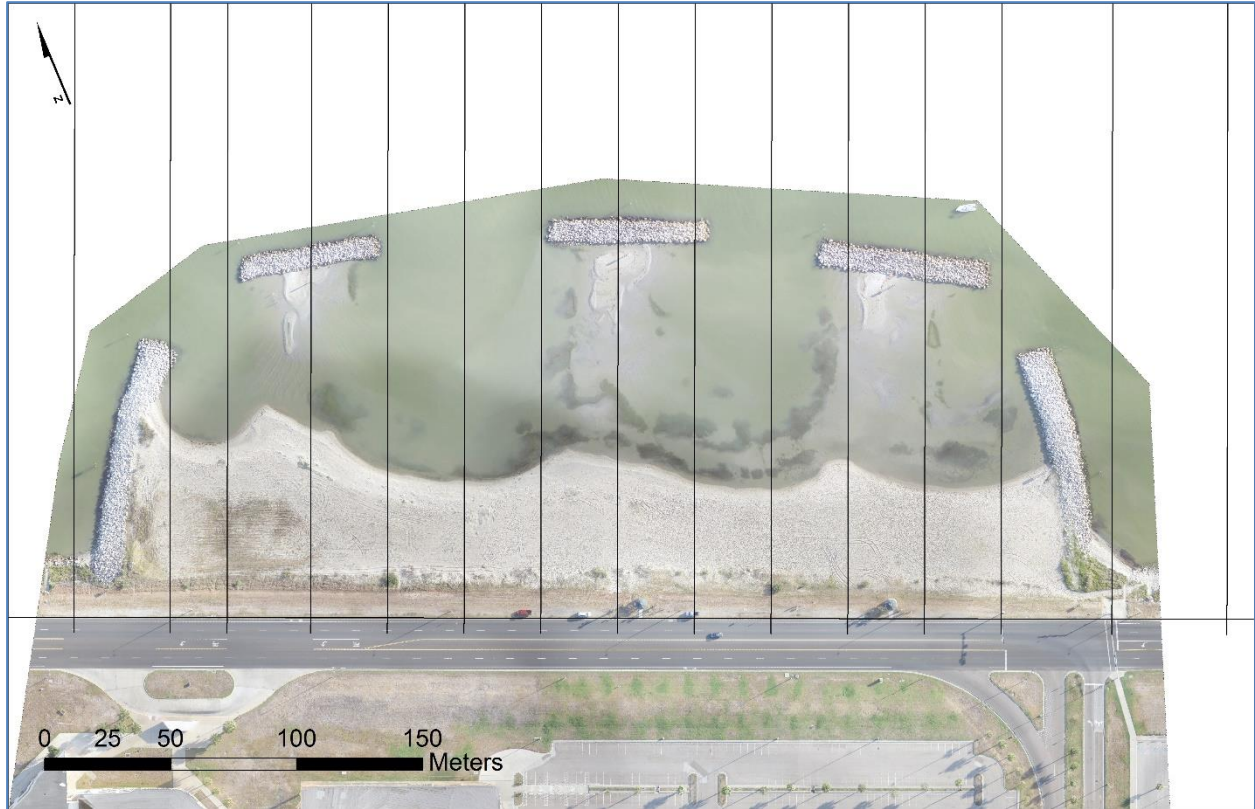
Figure 3.1: Survey setup: transects ran perpendicular to Ocean Drive and general shoreline orientation.

UAS Survey

The UAS used in this study was the Sensefly eBee, which is an ultra-light foam fixed-wing platform, with a wingspan of 96 cm (Figure 3.2). Weight with sensor payload is 0.69 kg. The eBee is propelled by a rear push propeller and powered by a lithium ion battery which provides approximately 50 minutes of flight. 12 km^2 can be covered with one flight (Sensefly, 2014). Onboard sensors include a GPS receiver, altitude sensor, inertial measurement unit (IMU), magnetometer, wind speed sensor, and a radio transmitter to receive and transmit data during flight navigation.

Figure 3.2: eBee launch and scale. Former student launching eBee UAS at TAMUCC campus.

The eBee can be loaded with a flight plan, and also receives navigation data and commands via radio link. The eBee is capable of autonomous flight. A computer transmits the flight plan via radio link and the eBee navigates along the flight lines at a specified altitude using multiple sensor input and GPS location (Figure 3.3). Imagery was recorded using a Canon IXUS 127 HS with 16.1 megapixel CCD 6.16mm x 4.62mm, and a focal length between 4.3mm-21.5 mm (Cannon, 2013). The Canon IXUS 127HS is a smoothed and filtered 3 band sensor: red, green, and blue.

Figure 3.3: Miniature GPS chipset: the miniaturization of GPS chipsets (shown) and inertial micro-electromechanical systems (MEMS) allow for a lighter platform for aerial photography. The chipset used in antecedent Sensefly models including the CAM Swinglet utilize an Arduino u-BLOX GPS chipset. Trajectory and position is processed and recorded at 1Hz. This geospatial information also allows the UAS to fly autonomously using input data to calculate and adjust navigation (Vallet et al 2011).

The TAMUCC Sensefly eBee drone was flown on August 24 and October 5, 2014 for the purpose of collecting multispectral imagery to be used in the production of 3D point cloud data, a digital surface model (DSM), as well as an orthomosaic using the SfM workflow. Table 3.1 presents a summary of flight parameters including meteorological conditions. Average water depth over project area was 33.5 cm (1.1 ft) + 13.7 cm tide August 24th flight and + 43.9 cm tide for October 5th flight or 42.7 cm (1.4 ft) and 77.4 cm (2.5 ft) respectively. Maximum depth in study area was 151.5 cm (4.97 ft) +/- tide values. The August 24th flight altitude was 24.97 m (81.92ft) less than the October 5th. (21.6%). The August

24th flight experienced 3 knots less wind at 7 knots versus 10 knots. Tidal level for August 24 was 0.30 m (1.0 ft) lower than tide level on October 5. Aerial targets were manually identified along said transects for use as manual ground control points (GCPs) in model coordinate transformation. The imagery was post-processed with Postflight Terra3D software which operates using embedded Pix4D software.

Table 3.1: Description of flight parameters and meteorological conditions.

Flight Parameters - August 24, 2014

Tide level (NAVD 88)	0.136 m (0.446 ft)
Temperature	84° f
Wind Speed	07 knots SSE
Visibility	16.1 km
Flight Time	8:15
Flight Duration	11 min
Altitude	90.53 m (297 ft)
Project	tamuccbeach_flight1_24aug2014
Processed	2014-Sep-29 22:35:01
Average Ground Sampling Distance (GSD)	2.92 cm / 1.15 in
Area Covered	0.25 km2 / 25.0019 ha / 0.0966 sq. mi. / 61.8129 acres
Ground Control Point (GCP) Coordinate System	NAD83 / Texas South (ftUS)

Flight Parameters - October 5, 2014

Tide level (NAVD 88)	0.439 m (1.442 ft)
Temperature	70° f
Wind Speed	10 knot SE
Visibility	16.1 km
Flight Time	8:30
Flight Duration	25 min
Altitude	115.5 m (379 ft)
Project	flight1_5oct2014
Processed	2014-Nov-01 22:52:39
Average Ground Sampling Distance (GSD)	3.56 cm / 1.4 in
Area Covered	0.8411 km2 / 84.1088 ha / 0.3249 sq. mi. / 207.945 acres
Ground Control Point (GCP) Coordinate System	NAD83 / Texas South (ftUS)

3.2 SfM Processing Workflow

The SfM workflow using the PostFlight Terra 3D software (i.e. Pix4D) is broken into 3 main steps: initial processing, point cloud densification, and DSM and orthomosaic generation. Refer back to Chapter 2 for more details on the SfM approach.

(Step 1) Initial processing of the photos extracts the interior and exterior camera orientation and develops a sparse model using features tracked across multiple photos. Initial processing sorts all of the photos using the GPS positions (though they are not a prerequisite), and then computes key points. Keypoints are prominent features that provide for efficient tracking across photos, such as measured using the SIFT algorithm. The sets of keypoints are correspondences identified using image coordinates in as many photos as they appear. An automatic aerial triangulation and bundle block adjustment are used to create the first projective reconstruction or 'sparse model.'

The projective reconstruction does not have a native coordinate system. The user must manually adjust to a coordinate system by introducing known real world coordinates. This is typically done in the software by identifying control targets within imagery (Figure 3.6). Prior to each flight, square black and white targets (0.61 m^2, 2.0 ft^2) were set out in a staggered orientation along said transects in order to use manual ground control points (GCPs) in model coordinate transformation (Figure 3.5). In addition, underwater control was used in order to facilitate model transformation in submerged areas shown to be problematic for automated matching algorithms (Figure 3.4). Targets were located and positions recorded using RTK GPS.

Figure 3.4: Target placement: 15 black and white aerial targets were placed in staggered orientation along 3 transects for use in the transformation between model and real-world coordinates.

PostFlight Terra 3D contains a tie point/manual GCP editor which allows the user to import the coordinates of the targets and identify them in photos for model reoptimization and transformation to real world coordinates. Initial processing creates the base model so that the densification process can be completed via projective reconstruction which takes groups of individual pixel correspondences as input and generates 3-dimensional location as output. RMSE was calculated for reprojection error of the manual ground control using the following methodology found in Pix4D Online Support website (Eq. 2).
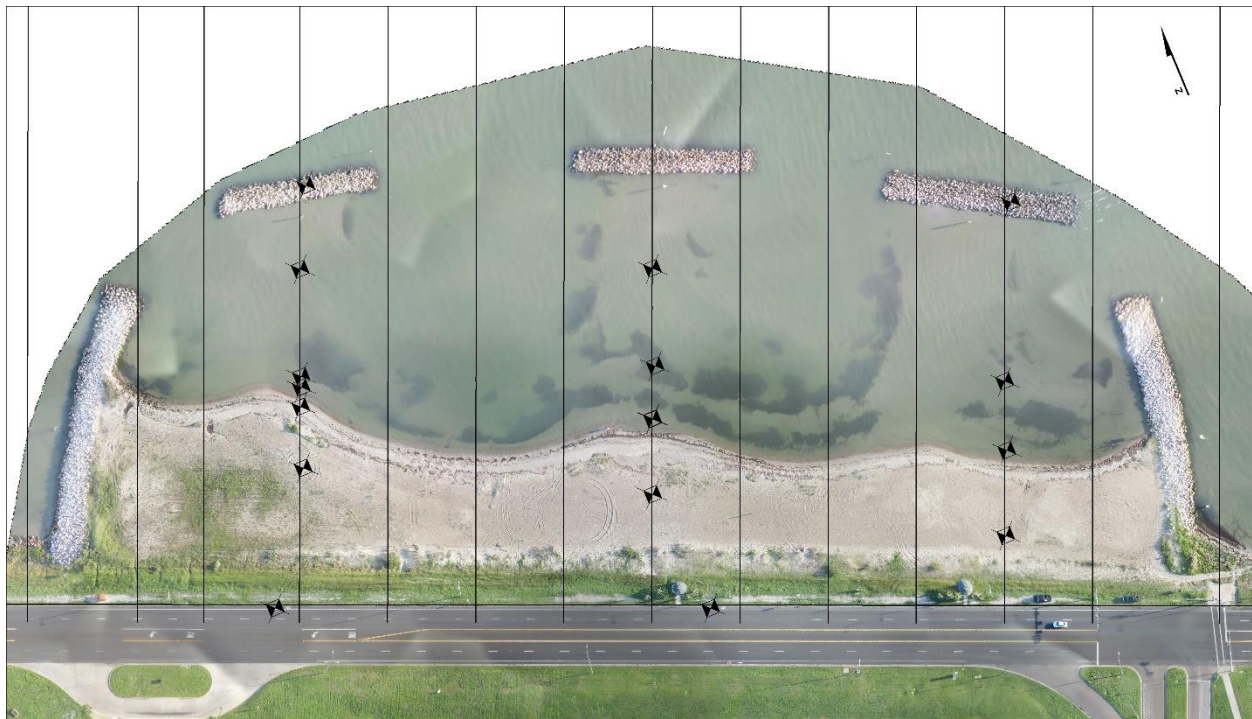
Figure 3.5: Aerial target setup (signalized control) for October 5, 2014 aerial survey.

IMG_3668.JPG
IMG_3694.JPG
IMG_3695.JPG
IMG_3701.JPG
IMG_3702.JPG
IMG_3703.JPG
IMG_3871.JPG
IMG_3898.JPG
IMG_3899.JPG
IMG_3905.JPG
IMG_3906.JPG
IMG_3907.JPG
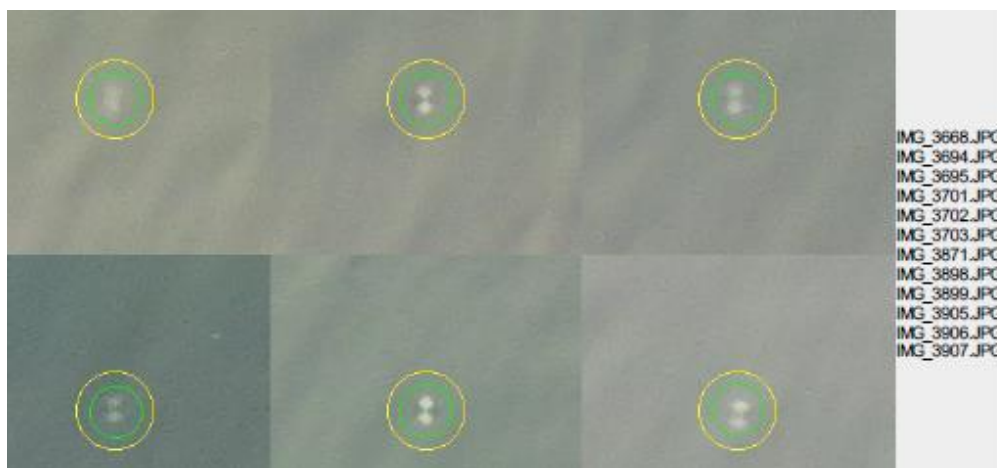
Figure 3.6: Submerged targets located in image coordinates

3-dimensional error estimation from tie points is the calculated residuals estimated to still exist

between measured tie point location in imagery and projected tie point location. Projection

errors exist after SfM model has been adjusted by least squares and transformed to a coordinate

system given the constraints imposed by matched features (or manually introduced features such

as targeted control). The difference between measured (manually identified) tie points is weighted by the 2-dimensional covariance Σ_i, and projection error for a particular image is:

$$e_i = (m_i - x_i)^\top \Sigma_i^{-1} (m_i - x_i) \text{ (Eq. 2)}$$

Where e = reprojection error vector of 3-dimensional coordinate in image i, x_i and y_i = 2-dimensional coordinate of measured control point, and m_i = the 2-dimensional coordinate of the projected control point (Strecha, 2014).

(Step 2) Point cloud densification is the next step in the SfM process. The densification process is typically performed by a process known as dense matching and uses the sparse model and initial estimates of camera orientation to reproject individual pixels in real coordinate space. The 3D point cloud that is produced is the primary objective of SfM. Point cloud densification was performed using default parameters including the use of a minimum of 3 match points for each solved 3-dimensional pixel location and the densification of 1/2 scale images. Higher match point constraints increase positional integrity at the cost of reduced point density. Image scale defines the scale at which 3-dimensional point cloud locations are computed for the returned point cloud. Default 1/2 scale is recommended for use in project areas that do not exhibit very high contrast with many sharp features such as cityscapes. Ultimately, final point cloud density is defined both by sampled image scale and by the point density parameter within Pix4D. The optimal default value was used for processing both datasets which computes a 3-dimensional point for every 4/image scale. Since 1/2 scale was selected, then a point was computed for every 16 pixels which optimizes processing, and imparts further constraint on final pixel locations by increasing the sample size. Default data output of LAS format was retained which enabled easy integration into LAStools and ArcGIS for further processing and filtering. The point cloud was analyzed by comparing RTK GPS observations along survey transects to individual constituents of the densified point cloud. Comparisons were analyzed of multiple point cloud outputs from Pix4D densification from the August 24 and October 5 flight dates.

Two densified point clouds were output per flight: a densified unfiltered point cloud and a radially filtered point cloud using built-in Pix4D noise filter, which is strictly a smoothing radius-based

filter. Smoothing determines outliers by identifying the median value within a user-defined radius distance. It is designed to remove noise, but will not identify badly matched areas, nor is it a ground point filter. Radial filters can remove more or less dependent on the radius, but over water where there were spurious returns, it performed poorly. The radius used as default within Pix4D is 10XGSD; for August 24 and October 5 flights the radial distance used was 0.292m and 0.356m respectively.

(Step 3) The final step in the Pix4D SfM workflow is the production of orthorectified rasters which can be produced from the 3-dimensional sparse model (initial processing) by populating a DEM with colors from pixels of the photographs covering that area (Figure 3.0 and 3.4). Images are projected using the estimated camera orientations. Colors are developed in Pix4D by blending calculated with weights given to photos based on distance from pixel to camera focal point (Pix4D, 2015). These orthomosaic and DEM SfM products were used later to export reflectance indices to be used in the optical inversion approach described on page 31.

3.3 SfM Point Cloud Post-Processing and Analysis

The acquired images are at very high spatial resolution with the resultant final orthomosaics featuring a GSD of 2.92cm and 3.56cm for the August 24 and October 5 surveys respectively. The produced point clouds for both flights were high density with average point spacing of 12.5cm (0.41ft) and 11.60cm (0.38ft) for unfiltered point clouds. Point spacing for the two flights averaged 3.8XGSD due to the 1/2 image scale constraints selected for the low contrast project area and the optimal default point density parameter. These parameters decrease the potential coverage of full resolution SfM 3-dimensional point calculation, but also significantly decrease time for processing and point analysis, and allow for further constraints in areas with little contrast (low texture) without sacrificing accuracy. Average horizontal RMS error from observed targets (RTK GPS) and SfM derived target x,y positional values was 2.2cm (0.075ft). LAS files and subsets were observed in LASview (rapidlasso GmbH, 2015) in order to quickly display entire point sets and assess visual inspection.   Areas over water were scrutinized, and it was evident from visual analysis that the October 5 data was excessively noisy with

some patches being reported at more than -20 m (-65 ft) NAVD88 which is far deeper than any of the recorded GPS observations. This stems from disparity in the pixel matching process over the dynamic water surface and mismatching due to specular reflection. The resultant mismatch causes spurious projective 3D coordinates (spurious elevations).

Spatial analysis was performed in ArcGIS 10.1 by comparing the RTK GPS observed elevations to the z-value of the nearest point produced in the SfM point cloud densification process. LAStools, a lidar data processing software suite composed of different command line modules was used for point cloud processing and DEM production from LAS point cloud files (Rapidlasso GmbH, 2015). In order to perform a robust 3-dimensional point analysis, three point groups from each flight were isolated for separate analysis including two sets of bathymetric points over or within the water surface, as well as the remaining terrestrial points. Bathymetric points were isolated using different methods. The first group of bathymetric points were all 3-dimensional points over and/or underneath the water surface. This point group was derived by using a 2-dimensional clip function with a 'water surface' polygon derived using the red-band threshold value between terrestrial and water reflectance values to delineate water level boundary. The 'water surface' polygon represented the area of survey inundated with tidal seawater at the time of survey. The water level contour was digitized by analyzing the isolated red band of the orthorectified reflectance map. The threshold reflectance value was determined to be 145 between terrestrial points and water surface returns using 3D Analyst (3-dimensional line interpolation) in ArcMap. The 'Set Null' tool was used to eliminate raster values greater than the threshold value leaving the majority of data over water, and allowing for the indiscriminate delineation of a 'water surface' polygon for the project area. Both August 24th and October 5th orthomosaics were also visually inspected and checked against water level GPS observations along the survey transects in order to verify reflectance map 'water surface' results. Clipping LAS files with the 'water surface' polygon was performed via 'LASclip' and called '*Sub-surface_Clip*'.

The second bathymetric point set for each flight was derived by isolating all points from the final point cloud with elevations equal to or less than the recorded water level at the time of flight. This method

was performed using a Python script which read in lines from the LAS-derived XYZ ASCII data, isolated those points with z-value less than water level at the time of aerial survey, and then recorded those XYZ positions to a new file. LAS coordinates which were of elevation less than water level at time of flights 13.72cm (0.45ft) NAVD88 (Aug 24) and 43.89cm (1.44ft) NAVD88 (Oct 5) respectively were selected and recorded. The points were labeled '*Sub-surface*'.

Terrestrial points were separated using a reciprocal and adjacent polygon to the respective water surface polygons. Terrestrial points were labeled '*Terrestrial*'.

SfM Vertical Accuracy Assessment:

Initially, spatial statistics for LAS point clouds were computed using LASinfo (a LAStools module), which produces a text file of some basic spatial parameters of the point cloud such as point density and average point spacing. The relationship was then analyzed between RTK GPS observations and nearest LAS point for all three described datasets. A spatial join was performed in ArcMap on the original RTK GPS observations in order to join data from '*Terrestrial*', '*Sub-surface_Clip*', and '*Sub-surface*' point sets. The spatial join was accomplished using a search radius of 0.914 m (3.0 ft) to find the closest LAS point. Since point spacing for both flight dates averaged 12 cm, the search radius of 3.0 ft was only needed where a GPS observation was appropriate for comparison to the nearest patch of data over water. The search radius was not required over sub-aerial beach which had nearly complete coverage. Next, the resultant data sets had to be manually cleaned because the radial search for bathymetric points included some fringe terrestrial RTK GPS observations and vice versa. To calculate statistics, each attribute table was exported and manipulated in Microsoft Excel. Residuals were calculated by taking the difference of SfM LAS point z-value from the RTK GPS observed elevation. Statistical information on residual error versus depth of water cover was calculated and reported in Appendix B.

Slope of the terrestrial beach surface was extracted to analyze its effect on SfM-derived vertical elevation measurements (i.e. due more sloped parts of the beach exhibit more error in the vertical component of the point measurement). First a $0.61m^2$ DEM was created from the RTK GPS observations

by using the "Topo to Raster" geoprocessing tool. The "Surface Slope" tool was then used with the

0.61m^2 DEM as input and degrees slope for raster value of the output. Slope raster values were appended

to the terrestrial point dataset using the ArcGIS tool "Extract Values to Points" tool.

Vertical error of SfM points over water:

Many point cloud z-values derived from water surface correspondences were prone to error.

Many, if not most, of the match points appear to have been created from ripples on top of the shallow

water or white light reflected off the crests of wavelets (glint), and are not produced from light reflecting

off of the sub-surface bottom. As a result, some of the data produced using SfM workflows contained

areas of inaccurate data (Figure 3.7). One of the goals of this research was to address problems

encountered with using SfM over water. Erroneous matching during initial processing as well as the

dense matching process were commonly observed over water. The filtering methods below were aimed at

trying to mitigate for these effects on the October 5 dataset.

The bulk of inaccuracies were clustered so that the radial Pix4D outlier filter was not effective.

Since neighboring values were often incorrect as well, the clustered noise did not produce outlier

characteristics which could be identified by a 2D moving window or radial filter.
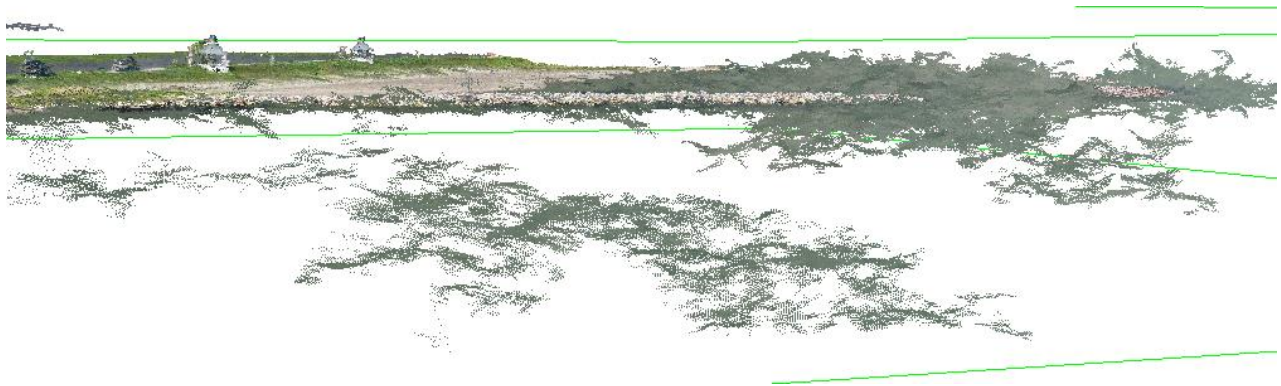
Figure 3.7: The October 5 unfiltered point cloud contains z-values as low as -21.44m (-70.33ft) and as
high as 10.34m (33.92ft)

The strategy used to filter and rectify the October 5 dataset was based on a method called

"Removal of Cloud Returns with a Coarse DTM" (Isenburg, 2014). The method was developed to filter

airborne lidar point cloud data. It utilizes a coarser resolution surface, such as those produced by NASA's

Shuttle Radar Topography Mission (SRTM), as an initial reference surface in order to trim maximum and

minimum values from the airborne point cloud of interest in order to eliminate false lidar returns, such as

cloud hits. For this research, a reference surface was temporarily created from the same eBee UAS/SfM

derived point cloud dataset. In order to create a relatively accurate surface from the data already

collected, an alternative processing technique was employed whereby different parameters were chosen

for the point cloud densification step of the Pix4D SfM workflow. Instead of using a 3-match minimum

per pixel coordinate identification, densification was performed using 4 and 5 minimum matches per pixel

(two datasets) (Figure 3.8). This resulted in a less dense set of points, but typically the remaining points

were less prone to error. Though the 4-match point cloud contained less error than the unfiltered dataset,

large areas of erroneous data persisted. A patch of excessively low elevation existed between the sub-

aerial beach and the center separated breakwater for 3-match and 4-match dense matching constraints.

The 5-match point minimum parameter mitigated the remaining inhibiting error clusters. 'LASnoise'

routine from RapidLasso (described below) was run on both of the alternatively processed and filtered

point clouds.
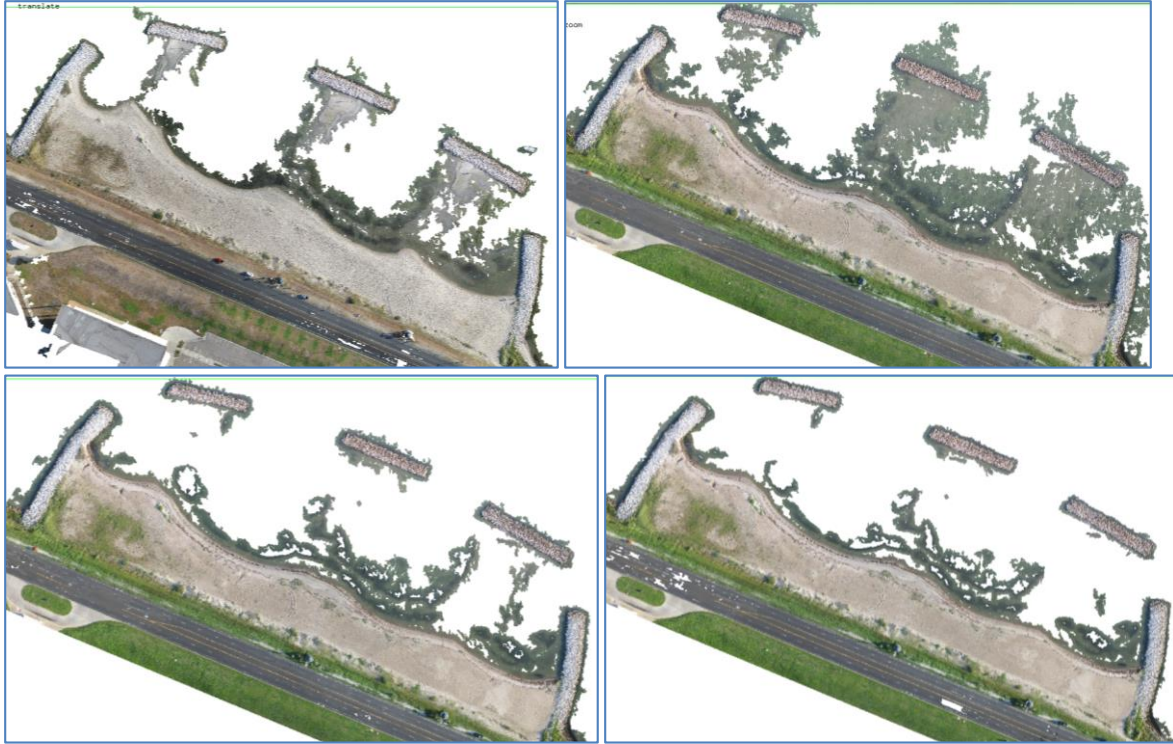
Figure 3.8: Overview of University Beach Coverage: The above results show various outputs from the August 24 and October 5 datasets. Top left: August 24, 3-match default densification radially filtered, top right: October 5, default densification radially filtered dataset. Bottom left: 4-match minimum densification; bottom right: 5-match minimum densification. Area is severely reduced as a result of imposing additional match point constraints.
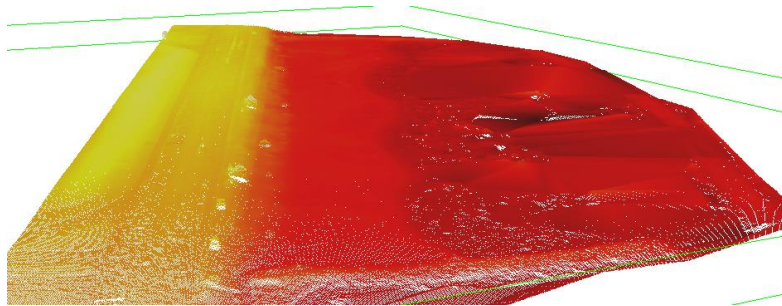
Figure 3.9: The TIN surface used as a clip reference surface interpolated from October 5 flight using a 5-point minimum match constraint. Note the patch of low elevations in dark red near the offshore center of the model that persists throughout all October 5 datasets - though mitigated for in this 5-match minimum.

'LASheight' from the LAStools processing suite was used to isolate and discard heights above

0.61m (2.0ft) and below -0.61m (-2.0ft) of a TIN surface of the 5-match minimum alternative processing

technique. LASheight computes height above a reference surface and gives the user the option to discard

32

any point data outside of the given thresholds. A surface distance of 0.61 m (2 ft) was chosen based on an iterative visual analysis using LASview to observe effects of various surface distance parameter clips and based on the average water depth of the project site during the October 5 flight of 0.774 m (2.5 ft). LASheight builds a temporary TIN surface from a user defined point cloud set (Figure 3.9). The output from LASheight was fed through LASnoise which enables the user to build a 3-dimensional moving window that identifies isolated values by applying user-defined parameters. The window is composed of the 27 surrounding cells along a 3-dimensional grid; each cell of specification given by the user. Since the goal was to try and remove clusters of outliers, a relatively small volume window was used which measured 0.61m horizontally (xy) and only 0.30m (1ft) vertically (z). LASnoise was run twice consecutively on the October 5 unfiltered point cloud. LASground was run on the LASnoise output which classified 1,585,104 points out of 5,237,184 as ground points. The final classified model was labeled '*Denoised*'(Figure 3.10).

Figure 3.10: '*Denoised*' workflow

The same three point group delineation was performed on the alternately processed 4-match and 5-match minimum point clouds for further analysis. Finally, a DEM of the '*Denoised*' point cloud was interpolated using LAS2DEM which populates a raster from a temporary TIN of the '*Denoised*' ground point data. A resolution of 0.30 m (1 ft) was chosen for final DEM in order to introduce some smoothing.

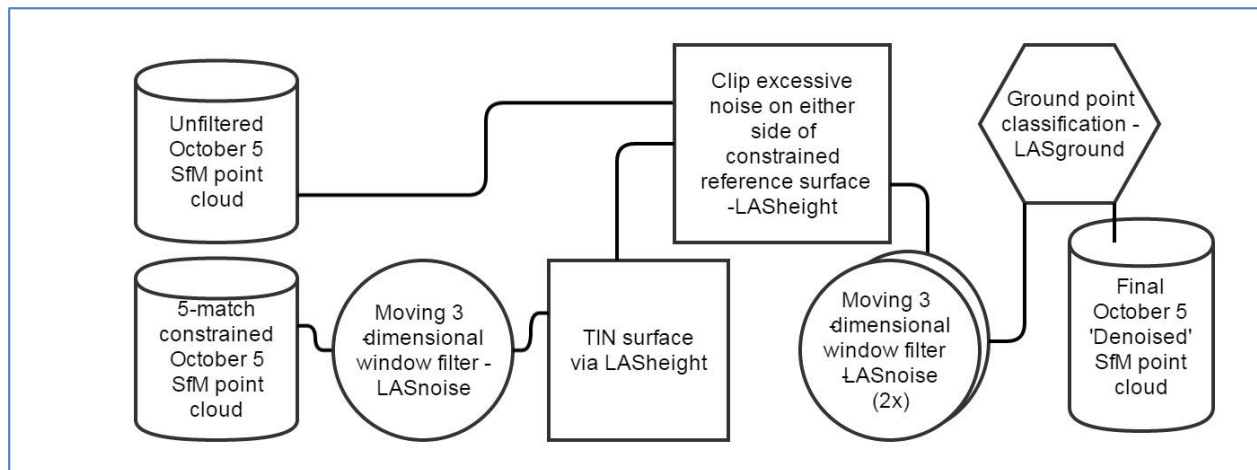## 3.4 Optical Inversion for Water Depth

An optical inversion approach was analyzed in this research in order to assess a potential alternative method to extract the water depth as opposed to the SfM point cloud, which experienced issues with sparse matching of high fidelity bottom returns. A variation of the OBRA methodology as described in GEBCO (2014) was generally followed using reflectance maps produced from SfM workflow on RGB eBee imagery. The orthomosaics produced using Pix4D utilize an algorithm that derives color for each pixel of the final output using dense-matching rules in combination with a DEM of the surface. The DEM is used in order to calculate whether or not a pixel (ray) from a photograph contributing to the model in that particular area is in fact completely visible from a particular location. If a particular pixel is providing information for the color of the final model, then a system of weights is used which blends multiple values from different photographs depending on distance from pixels to camera focal point. In this research imagery from the August 24th flight was used for optical inversion because of the superior radiometric qualities encountered as a result of calmer meteorological conditions. The August 24th optical inversion dataset was carried forward for use in the hybrid model because the lower tidal level allowed for the population of wet beach boundary by filtered SfM point cloud data which was found to be of higher accuracy along this zone.

In this study, the Canon IXUS camera used in image acquisition only recorded data in smoothed and filtered Red, Green, and Blue channels (RGB). Several ratios using these recorded color bands (i.e. Green/Blue) were assessed and tested for use with OBRA methodologies. Reflectance maps for each color band were produced using Pix4D Index Calculator which uses a combination of the weighted average and the multi-band blending algorithms (Table 3.2) (Pix4D, 2015). The index calculator loads point cloud data and generates DSM tiles with RGB reflectance information. The intention of the reflectance values are to derive the physical properties of the surface at a particular location.

Table 3.2: Reflectance Map - August 24, 2014
Resolution: 2.93 cm

Band	Min	Avg.	Max.	Std Dev.	Var
Red	6.00	131.760	255	41.97	1761.2
Green	6.85	133.230	255	38.01	1444.88
Blue	2.00	122.250	255	40.76	1661.04

Index mosaics were created in Pix4D by computing each pixel using a formula which combines the bands from the reflectance map produced earlier. Various combinations of bands can be used when computing indices. Since most of the post-processing was completed using ArcMap, only the single band indices were calculated in Pix4D index calculator. The individual color band (RGB) indices from the August 24 flight were used to attempt the optical inversion approach discussed in Section 2.4 because calmer meteorological conditions resulted in a smoother water surface with less suspended solids throughout the water column. The wind speed was minimal at only 7 knots and the photos were taken at a lower altitude and thus had more resolution (2.92 cm GSD). It is hypothesized and assumed for this research that more light would pass through the water and be returned to the camera sensor on days with less wind due to less scattering from capillary waves on the water surface. Orthorectified reflectance indices were exported directly from Pix4D reflectance index calculator. Since the Canon IXUS 127HS produces imagery in 3 bands, one index of each band was produced and exported in TIF format.

Guidelines from NOAA's GEBCO manual were followed in order to process combinations of reflective indices for optical bathymetric inversion (GEBCO, 2014). The optical inversion approach uses the OBRA equation (Eq. 1) discussed in Section 2.7. ArcMap 10.1 was used primarily with the geoprocessing tool raster calculator to apply map algebra operations to perform the bathymetric inversion equation using raster division and calculation of the natural log.

The first step in the optical inversion process was to isolate points that were recorded over/through the water surface. For this process, the red band was relied upon as an indicator of the presence or absence of water. Because red light is more readily absorbed when passing through water, it was assumed that red band energy registered at the camera sensor would be a result primarily of reflection

from the surface of the water and not transmission from sub-surface substrate. As such, the '3D analyst'

toolbar within ArcMap 10.1 was used in order to interpolate the reflectance values of the red band index

raster along a line drawn from the sandy beach, across the shoreline, and terminating in water cover

approximately 1.25m in depth. The reflectance values were graphed along the profile and the threshold

value of 145 was identified as a suitable value representing the sudden transition of high reflectance over

terrestrial returns (>180) and the lower reflectance values returned from the water's surface (<140)

(Figure 3.9). The "Set Null" tool within ArcMap 10.1 was used in order to nullify terrestrial values (non-

water surface returns) (Figure 3.11).
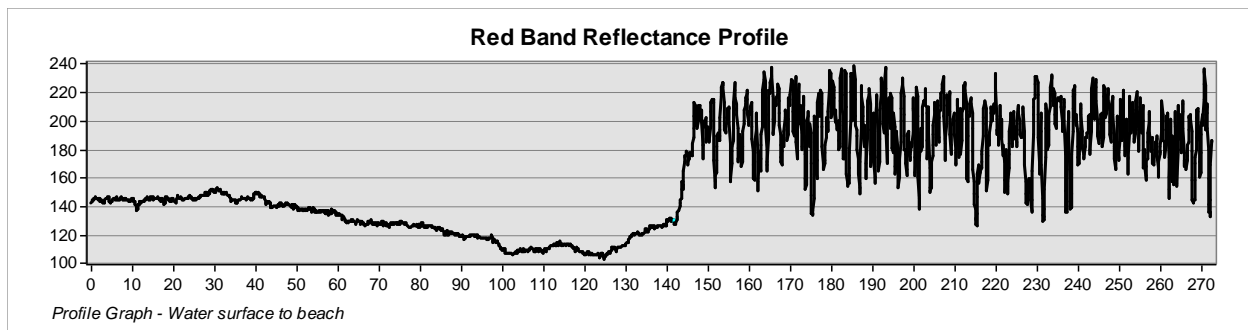
Figure 3.11: Optical inversion data analysis: clip water surface points by using 3D analyst and interpolating a line drawn from water to land. The abrupt value changes represent transition from water to land.
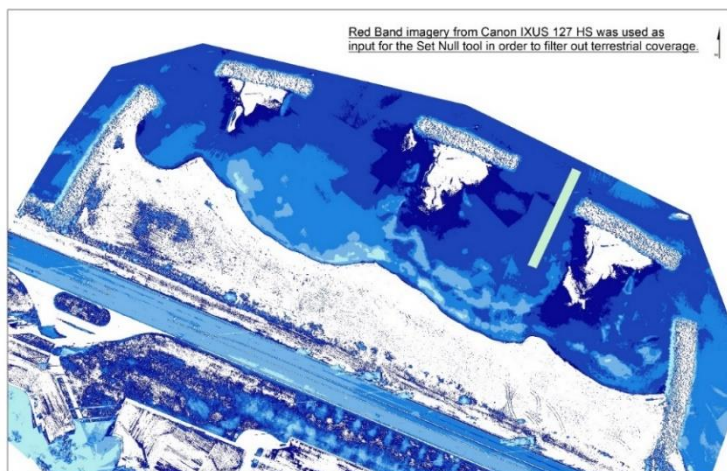
Figure 3.12: The resultant raster represents water only surface for the red band which was used in other "set null" operations as the clipping raster for the remaining Blue and Green rasters. Rasters that represented reflectance values over water were required in order to implement the optical inversion algorithm as well as other 3D point analysis. The thin rectangular polygon between the middle and right breakwaters was used to extract RBG reflectance values for use in the normalization of the blue and green bands.

The red band index was also used to normalize the other bands and attempt to reduce interference from reflections off the water surface due to clouds and other factors. The red band was chosen for filtering since red wavelengths of light are more heavily absorbed while passing through water relative to the alternative green and blue wavelength bands. To implement the red band filter, first a polygon 60.40m (208ft) X 5.70m (18.69ft) was drawn over a thin strip of area that extended over the water from 47.5m off the shoreline at 0.30 m of water cover out to approximately 1.25m of water cover. The particular area was chosen because the substrate was visibly observed as sand bottom so that clay/seagrass substrate anomalies within the survey area wouldn't affect reflectance values. A linear regression was used by comparing graphic plots of blue and green values versus red values. A linear best fit equation was calculated for the plot (Figure 3.13). Calculations produced normalized values for each band by implementing the regression equations.
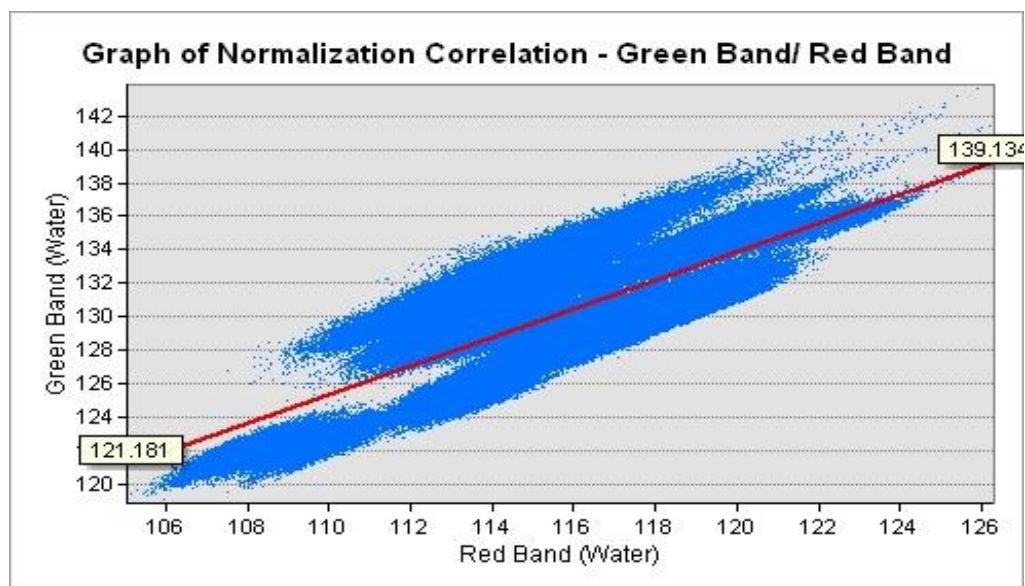
Figure 3.13: A linear regression is used to normalize blue and green bands by graphing plots of blue and green values versus red values.

'Normalized' rasters were output using 'raster calculator' in ArcMap to apply red band linear regressions. Rasters were then clipped using the 'set null' red band raster for water surface threshold and 'raster calculator' was then used in order to combine color bands.

37

Because it was unknown if inversion techniques were effective using smoothed bands captured by non-metric consumer cameras, the entire network of GPS observations were used as training data in order to obtain the most accurate regression fit between depth of water and substrate reflectance using the different band combinations (Eq. 2). Since GPS coordinates were already stored using the orthometric height above Geoid 2012a, the direct relationship was sought between band ratios and elevation in NAVD88.

$$\text{Depth (Elevation NAVD88)} = m_0 \frac{\ln(R\lambda 1)}{\ln(R\lambda 2)} + m_1 \quad \text{(Eq. 2)}$$

The goal was to identify the best-fit relationship between band ratios and depth of water. Additionally, individual band reflectances as well as a raster of the average of all three bands were analyzed against elevations in order to identify any potential correlations. These ratios of color bands as well as single color band rasters were analyzed against GPS observations using 'extract value to point'. Microsoft Excel was used in order to analyze the exported attribute tables. Raster values were plotted over observed NAVD88 elevation in order to identify correlation between reflectance properties stored within smoothed bands of the camera and depth. The natural log ratio $\frac{\ln(Blue-450nm)}{\ln(Green-520nm)}$ was found to exhibit the highest degree of correlation between reflectance ratios and observed elevation data.
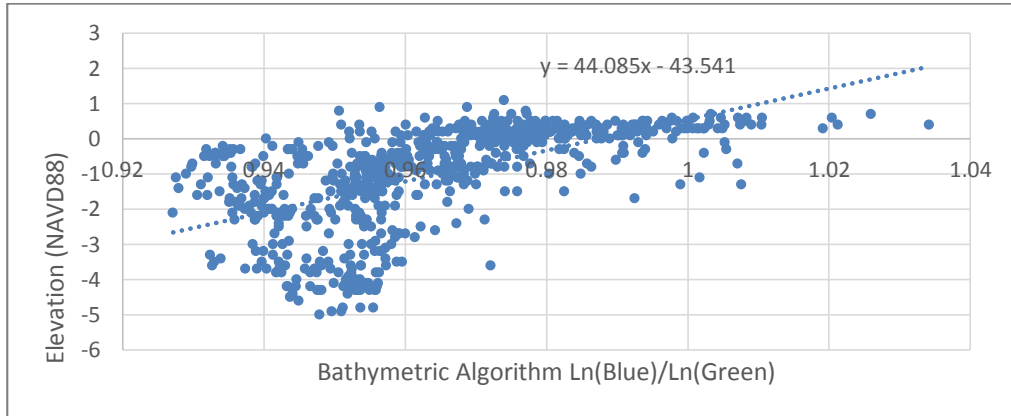
Figure 3.14: Graph of Bathymetric correlation between natural log band ratio $\frac{\ln(Blue-450nm)}{\ln(Green-520nm)}$.

This ratio is recommended in GEBCO when manipulating Landsat imagery over water. Results of each analysis and graph can be found in Results (Section 4.1). Finally, a simple linear regression was

performed via ArcGIS 'raster calculator' in order to convert raster values to depth values based on a best-fit equation (Figure 3.14).

3.5 Hybrid Surface Model

The final topo-bathymetric model of the sub-aerial beach and submerged topography created was a hybrid DEM fused together based on a combination of the SfM non-filtered terrestrial point cloud, filtered ('*Denoised*') water bottom surface point cloud, and optical inversion bathymetric measurements. Components were chosen based on RMSE analysis as well as the relationship between residual errors and depth of water which were used as an indication of accuracy. The October 5 filtered (Pix4D radial filter) '*terrestrial*' point cloud was used to interpolate a DEM for use in the hybrid model with reported RMSE value of 0.215m (0.70ft) and average residual value of 0.089m (0.29ft). Portions of the model over water were split out of two different sources. The '*Denoised*' LAS point cloud provided lower residuals (<1σ depth of water = 0.328m (1.08ft)) in depth of water cover less than 0.30 m than results from optical inversion derived from the August 24th data. Although the optical inversion algorithm utilized the entire network of GPS observations for calibration, the result was smooth and hydrologically correct. Average residuals were less than those reported from the '*Denoised*' filtered October 5 point cloud at water depth cover greater than 0.30 m – 0.80 m. The final hybrid model integrates the October 5 '*Denoised*' SfM LAS point cloud data along the shore where shallow water does allow for some accurate sub-surface densification (Figure 3.15). LASClip tool was used to drop points from the '*Denoised*' pointset with z-values below the 0.30m water cover threshold which coincided with the August 24th tide level. The hybrid model is a culmination of the work presented in this thesis. One weakness of this model is that SfM point cloud from October 5 flight is merged with bathymetric optical inversion data from August 24th flight. This is because hydrological and meteorological conditions during August 24th flight were more conducive to optical inversion (less wave action, less turbidity, less wind). The October 5 dataset was chosen for the source of SfM point cloud data because although the dataset exhibited more noise, the point cloud for October 5 covered more sub-surface bathymetry than the August 24th flight. A time

39

window of approximately 44 days occurred between these two aerial surveys; however, no significant change to bathymetry was expected below the tidal range. Historical data from TAMUCC Division of Nearshore Research Station 'Naval Air Station' (decommissioned in 2004) shows that the water level for Mean Lower Low Water (MLLW) is 0.036 m (0.12 ft) NAVD88. See section 3.6 for details on how water level datums are derived according to NOAA methodology. Since the tidal elevation was 0.134 m (0.44 ft) for the August 24th flight (approximately 10 cm above the lowest average of tides for 19 years), it was assumed that minimal change due to wave and wind action would have occurred below the August 24th tidal level.
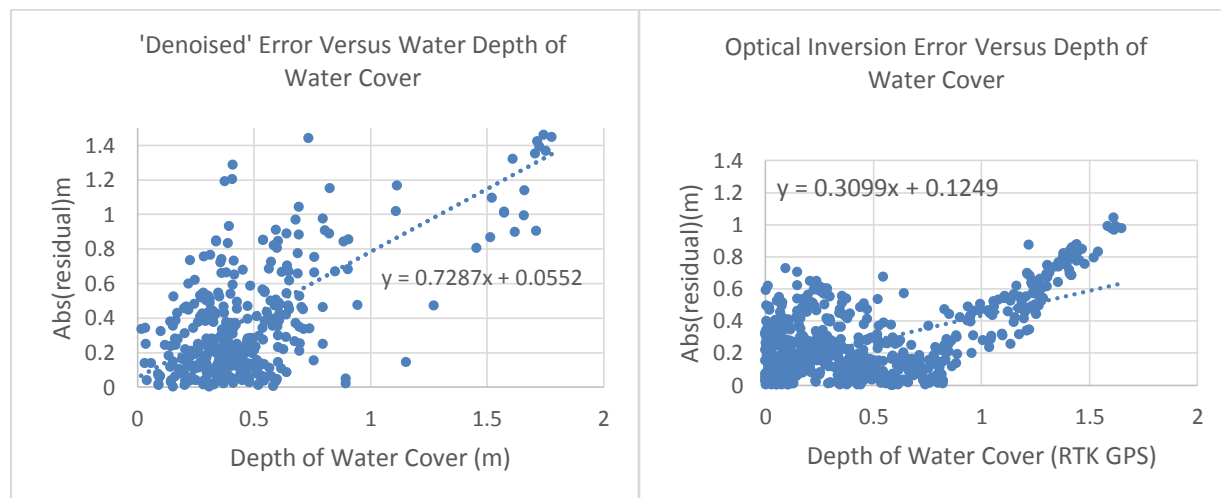
Figure 3.15: '*Denoised*' and Optical Inversion Error versus depth: The October 5 - '*Denoised*' LAS point cloud elevation data was used in the hybrid model from the edge of the 'terrestrial' point cloud dataset out to a water cover depth of 0.30 m (1.0 ft). The optical inversion DEM was used in the hybrid model from 0.30 m of depth of water cover out to the edge of reflectance map coverage. Left – October 5, '*Denoised*' - Absolute value of residuals (m) versus depth of water cover. Right – same relationship shown for the optical inversion raster.

3.6 Shoreline Contour Comparison

A portion of this research sought to quantify the accuracy of a MHHW contour extracted from the SfM point cloud data. The MHHW tidal level is found by averaging the highest of the diurnal tides from an epoch of 19 years of recorded tidal cycles (NOAA, 2003). The current National Tidal Datum Epoch is 1983 through 2001 (NOAA, 2015). A contour elevation of 0.50m (1.6ft) NAVD88 was used to represent the MHHW line along the project site. This elevation value is outdated, and is based on a tidal level from

a decommissioned TAMUCC Division of Nearshore Research Tide Station 001: Naval Air Station tide gauge (1992-2004) (Deidre Williams, Pers. Comm., 2015). The elevation was used in this study because this elevation is the currently accepted MHHW in a historical monitoring regime managed by the Conrad Blucher Institute monitoring project known as Coastal Habitat Restoration GIS (CHGIS) (Williams, 2005). This MHHW contour line was mapped on site using RTK GPS methodology (Section 3.1). 145 RTK GPS observations were recorded along the MHHW contour of the sub-aerial sandy beach as well as along the rock breakwaters at an average distance of 5.5 m (18 ft). ArcGIS was used to compare MHHW points observed using RTK GPS methods to the MHHW contour generated from the various SfM point clouds via temporary TIN in LAS2iso.

The field points were used to create a 3-dimensional polyline. Four MHHW contours were derived from DEMs created from the densified point clouds for each survey (Table 3.3). MHHW contours were created from the August 24th flight radially filtered point cloud and three point clouds from October 5 flight including '*denoised*' point cloud from Pix4D unfiltered point cloud, and filtered 4-match point and 5-match point minimum densification process options. Finally, a LAS point cloud was derived from the final hybrid composite DEM using 'LAS2LAS' tool and the MHHW contour was interpolated from this DEM as well. The 'LAS2ISO' tool was used to quickly render a shapefile of the contour at a specific elevation. Because some of the point cloud data contained noise, contours with lengths less than 152.4 m (500ft) were ignored.

To calculate residuals for the various MHHW contour renditions the 'Near' function was used within ArcMap 10.1. Each in-situ MHHW GPS observation was written a distance value from each MHHW contour from the various point clouds. Each output table was stored as a CSV file. To differentiate near table results that were seaward of GPS observations for MHHW, a polygon was drawn incorporating MHHW lines from various processes. Selection by location was used to select features which were within this polygon; thus all features selected were "below" actual values and a negative attribute was assigned to near value. A true average could then be calculated and position relative to the

MHHW truth line could be taken into consideration during analysis. An average of 127 locations were

sampled for each SfM contour line.

Table 3.3: MHHW contour sources for each of the contour lines analyzed against a control
contour defined in-situ using RTK GPS.

Date/Source	Filter/Processing	Notes
August 24	Radially filtered	(10XGSD radial filter = 0.292 m)
October 5	'*Denoised*' (Figure 4.3)	LASnoise, LASheight, LASground
October 5	Alternate Processing 1	(4-match minimum point cloud densification)
October 5	Alternate Processing 2	(5-match minimum point cloud densification)
Hybrid Model	Model at MHHW line is similar to '*Denoised*' pointset	slight changes due to raster transformation

4.1 GNSS versus SfM Point Cloud

Statistical analysis was performed on the August 24th flight (radial filter) and multiple point clouds generated from October 5th flight including a radially filtered point cloud, '*Denoised*' point cloud using various LAStools approaches (see Section 3.3), as well as two sets of October 5 data using the 4-match and 5-match minimum dense matching parameters (Table 4.1). Results indicate that despite imposing additional restraints, such as match point minimums and various filters to the final point cloud output, the general function of the Pix4D SfM workflow along the littoral boundary is a rigid process and external filtering does not remove all erroneous data. Analysis of SfM products were directly compared to GPS observations based on RTK corrections from Trimble's VRS network (Eq. 3). Five point SfM point clouds were assessed in comparative analysis including radially filtered point set for The GPS observational errors are introduced into all comparative analysis including the computation of residuals (Table 4.2). A vertical positional error of $\sigma_z = +/- 2.0$ cm was assumed for RTK GPS observations and this error, $\sigma_{uncertainty}$, represents the propagated uncertainty in our ability to compare SfM z-values to GPS z-values. The term 'residual', ε, as used in these results refers to the difference between the RTK GPS z-value and the SfM-derived z-value.

Residual = GPS_z - SfM_z (Eq. 3)

Table 4.1: Total SfM points by dataset

Data set	Total Points	Water Surface	Terrestrial
August 24 - Radial Filter	**7,547,058**	578,681	6,968,377
October 5 - Radial Filter	**4,232,744**	1,017,246	3,215,498
October 5 - '*Denoised*'	**5,237,184**	683,728	4,553,456
-Ground Only	**1,585,104**		
October 5 - 4-match min.	**3,230,080**	564,906	2,665,174
October 5 - 5-match min.	**2,988,999**	467,752	2,521,247

The horizontal RMSE from observed aerial targets for the August 24 flight was 1.7 cm. The

horizontal RMSE from aerial targets for the October 5 flight was 2.7 cm for average of 2.2 cm.

Sub-Aerial Beach – 'Terrestrial' SfM point clouds:

Table: 4.2: Accuracy assessment over sub-area beach was represented by 'terrestrial' point clouds.

Sub-Aerial SfM Point Cloud Residual (ε) Comparison (cm)

Date	Processing	Average(ε)	σ
August 24	Radial Filter	5.6	15.5
October 5	Radial Filter	8.9	19.5
October 5	'Denoised'	10.1	22
October 5	4-match constraint	7.1	19.9
October 5	5-match constraint	6.9	19.9

Accuracy was shown to slightly degrade with increased slope which ranged from 0 to

approximately 20 degrees within the project area.
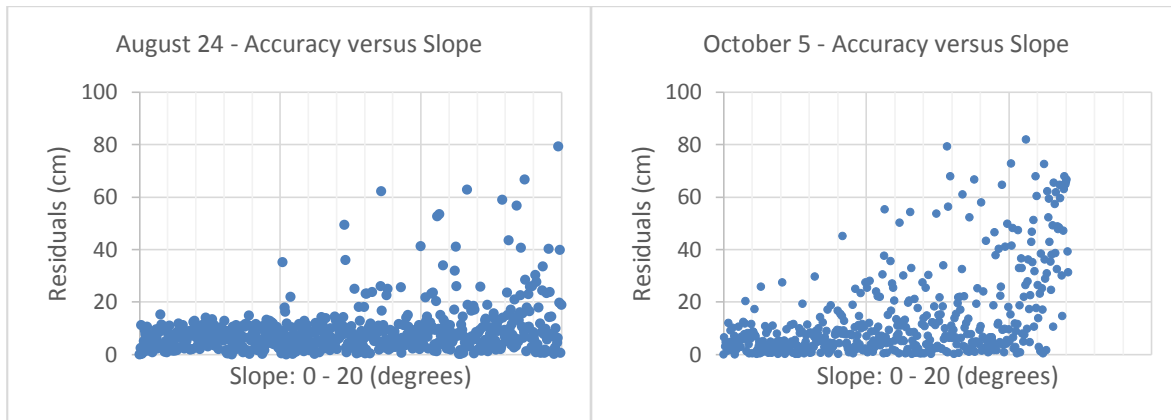
Figure 4.1: Accuracy versus slope for terrestrial SfM. Accuracy does degrade for some locations as slope increases; however, this can be attributed to an abundance of unmaintained vegetation.

The October 5 flight produced the noisiest unfiltered dataset with a standard deviation

exceeding 3.36m (12 ft) for residuals between SfM 3-dimensional location and the network of

RTK GPS observations (Figure 4.1).
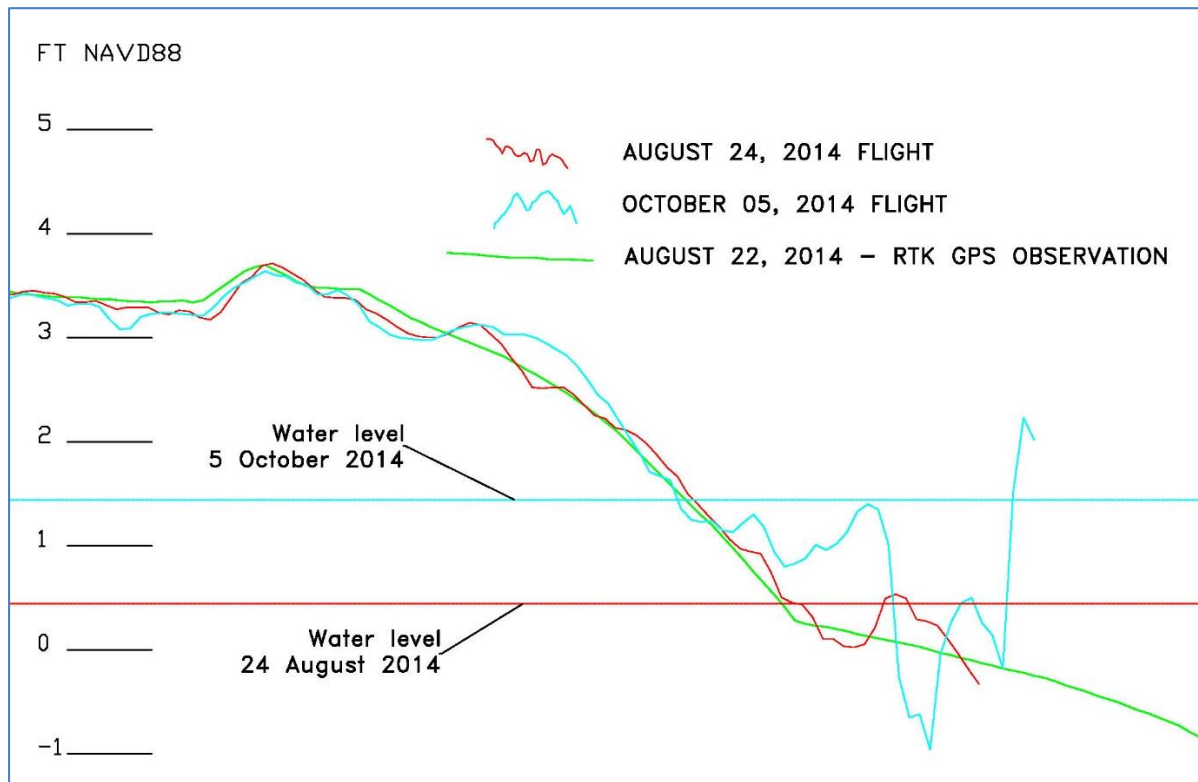
Figure 4.2: Typical section plot along transect showing radially filtered point data from August 24th and October 5th flights. The SfM profiles start to diverge from GPS trothing data below the water surface. October 5th flight data shows diversion approximately 1 ft (0.30) meters below water surface. This information to decide which datasets were compiled in the hybrid model.

Interest was shown in attempting to filter the October 5th dataset because although exhibiting relatively

large areas of noise, the area of coverage over water was more extensive compared to August 24th point

cloud (Table 4.3). Figure 4.2 is a cross sectional profile showing the effects of the water's surface on a

TIN surface rendered from a SfM point cloud in CAD.

Table 4.3: Comparison of areal coverage for 5 SfM point cloud datasets.

Areal Comparison of SfM Point Clouds

Dataset	Meters Squared
August 24 - Radial Filter	63,817
October 5 - Radial Filter	73,218
October 5 - '*Denoised*'	67,302
October 5 - 4-match constraint	61,429
October 5 - 5-match constraint	58,663

Bathymetric SfM Point Cloud Analysis:

Table 4.4 summarizes results of SfM solutions over water. The average depth of water cover in the area

of SfM point cloud generation was 0.47m (1.54ft) and 0.91m (2.98ft) for August 24 and October 5,

respectively. The overall average of residuals over water is -0.07m (-0.23ft). Average of overall

standard deviations over water was 1.0 m (3.26ft). Generally, the points over water were spurious returns

from the surface; however, the slightly negative trend reported (-0.23 m) is the result of some extremely

low values found in the October 5th unfiltered dataset where clusters of severely erroneous data exhibited

values as low as -21.44 m (Figure 4.3). The overall standard deviation of 1.0 m over water illustrates the

extreme variance and imprecision of the SfM point clouds over water. Without the addition of processing

constraints or filtering the SfM z-values over water are almost useless information.
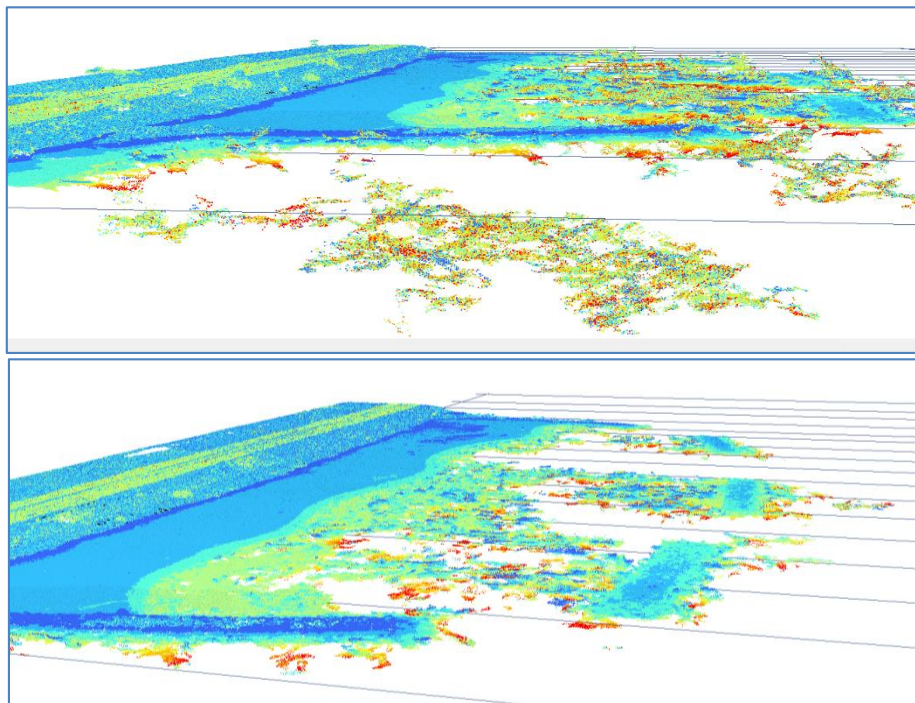
Figure 4.3: Top: October 5 - Unfiltered LAS point cloud. Glint and wavelets from increased wind, higher flight altitude, and a 0.30 m (1.0 ft) tide level increase relative to August 24 flight produced a much noisier point cloud over water. Bottom: October 5 - LAS point cloud after filtering using reference surface and moving window. Filtering was accomplished using LAS tools (LAS height, LAS noise) and classified using LASground.

Table 4.4: Sub-surface SfM Point cloud comparison

Sub-Surface SfM Point Cloud Residual (ε) Comparison (cm)

Date	Processing	Average(ε)	σ	Average Water Depth
August 24	Radial Filter	5.6	28.2	11
October 5	Radial Filter	-129.9	354.8	56
October 5	*'Denoised'*	-31.0	28.4	47
October 5	4-match constraint	9.4	28.8	40
October 5	5-match constraint	9.4	28.2	37

Appendix A shows a breakdown of the average water level where residuals were less than

(0.03m) 0.2' which is generally accepted survey-grade error. Water depth within this survey-grade range

averages 0.16 m (0.52'). Appendix B features a table of water depths and residuals broken down in

classes by standard deviation of residuals.

4.2 Optical Inversion

The optical inversion gave promising results. A simple linear regression of the final natural log

ratio $\frac{\ln(Blue-450nm)}{\ln(Green-520nm)}$ raster values to entire network of 735 GPS observations resulted in an average

absolute value of residual of 0.082 m (0.27 ft); however, standard deviation of 0.354 m (1.16 ft) indicate

relatively high variance in accuracy of bathymetry from optical inversion (Figure 4.4). Of course, such an

extensive network negates the goal of the optical inversion algorithm, but it does shows that the algorithm

can provide information through relationships between the reflectance values determined from weighted

smoothed bands and actual depth of water cover. The surface is smooth with clear transition from

shoreline to depth of extinction (approximately 0.8m (2.62ft)). For noisy datasets optical inversion might

provide an alternative for complete coverage of bathymetry. See Figure 3.15 in Methods for plot of error

over water depth of coverage.
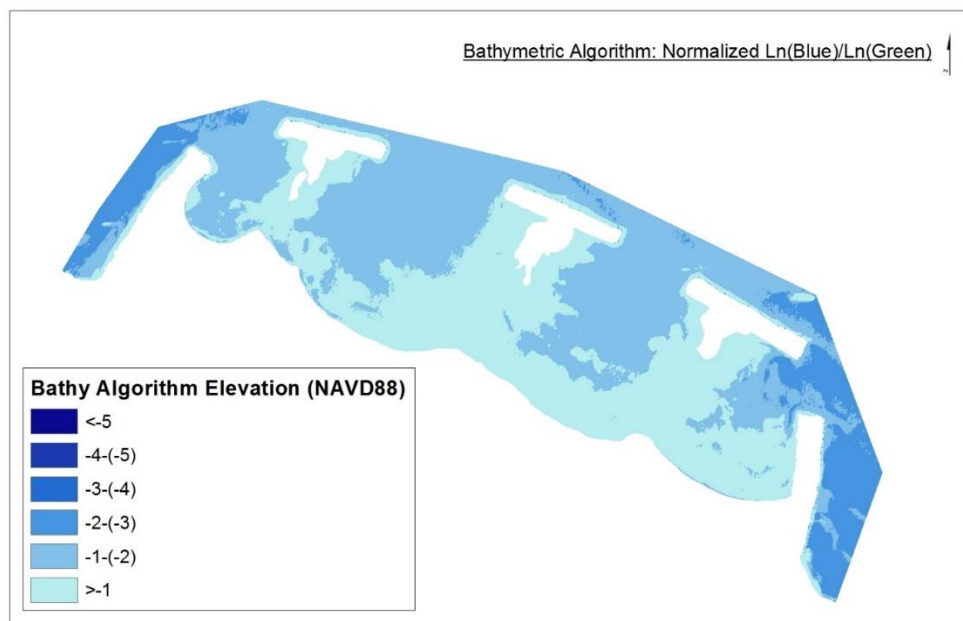
Figure 4.4: Final DEM created from bathymetric optical inversion. Best fit model was the red band normalized natural logarithm ratio of blue and green bands. The depth of extinction was approximately 0.8 m (2.62 ft).

4.3 Seamless Hybrid Topo-Bathymetric Model

The hybrid model (see Section 3.5) of the exposed beach and littoral zone (shallow water submerged part of the beach) combines the clipped areas of elevation data where processing produced relatively accurate results using the October 5 point cloud datasets and optical inversion results from August 24th flight. The purpose was to design a final model from SfM point data derived from submerged areas of interest. The October 5th dataset was chosen in order to propose a solution for merging multiple UAS derived products including an optical inversion bathymetry raster. The motivation was a focus on attempting to extract useful information from the October 5th dataset that covered more area.

For the sub-aerial beach, the radially filtered terrestrial points were used from upland to the shoreline on October 5th (elevation 0.439m (1.44ft) NAVD88). Carrying the model seaward through zero depth of water cover to approximately 0.30 m (1.0 ft) of depth of coverage, the October 5 '*Denoised*' dataset was used in the DEM using the 5-match reference surface (Figure 4.6). The hybrid model had an overall vertical RMSE value of 0.215m (0.70ft) and average residual value of 0.089m (0.29ft) for the entire area (Figure 4.5). Although the filters were very successful in reducing variation and bringing the average residual closer to zero, the filtered point set still trended +0.293m (+0.96ft) which lends to the

hypothesis that despite aggressive filtering techniques, most SfM coordinates over water are the result of incorrect water surface image matching.
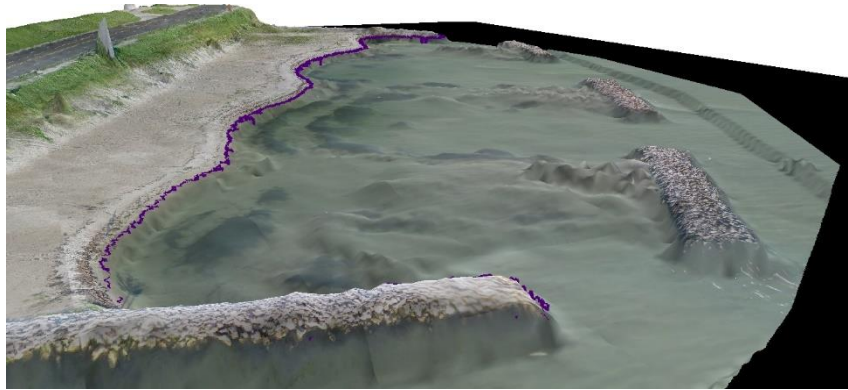
Figure 4.5: Hybrid model rendered in ArcScene - final hybrid model was composed of radially filtered '*terrestrial*' points, '*Denoised*' sub-surface points, and optical inversion DEM for seafloor bathymetry.
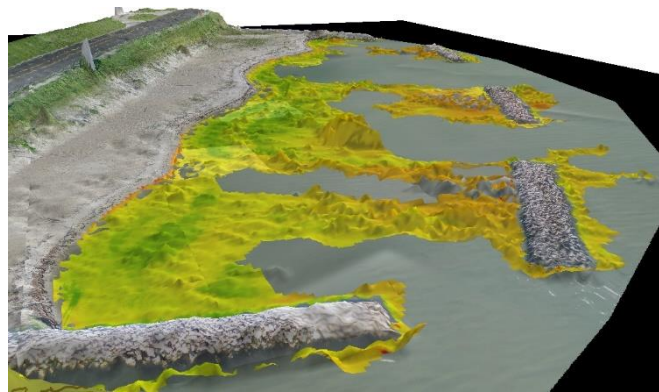
Figure 4.6: Hybrid model (natural color) plus October 5 '*Denoised*' LAS dataset overlayed. Both datasets are shown with a 3:1 exaggeration of height. Figure gives a visualization of the effects of poor image matching over water. Most of the SfM coordinate solutions over turbid water are water surface returns.

4.4 MHHW Contour Analysis

Contours were analyzed by using the 'Near' geoprocessing tool in ArcMap to write lengths between the GPS observation along the real MHHW contour and the derived SfM contour from DEM (Table 4.5). Locations where the SfM contour lay bayward of the control line were considered 'below' control line and given a negative value. MHHW contour derived from August 24 radially filtered produced the closest line to the control contour with an average residual of 0.240 m (0.79 ft) (Figure 4.7).

Table 4.5: MHHW Contours

MHWH Contour from SfM Point Cloud Residual (ε) Comparison (m)

Date	Processing	Average(ε)	σ
August 24	Radial Filter	-0.24	0.483
October 5	*'Denoised'*	0.515	1.879
October 5	4-match constraint	0.446	1.919
October 5	5-match constraint	0.561	1.860
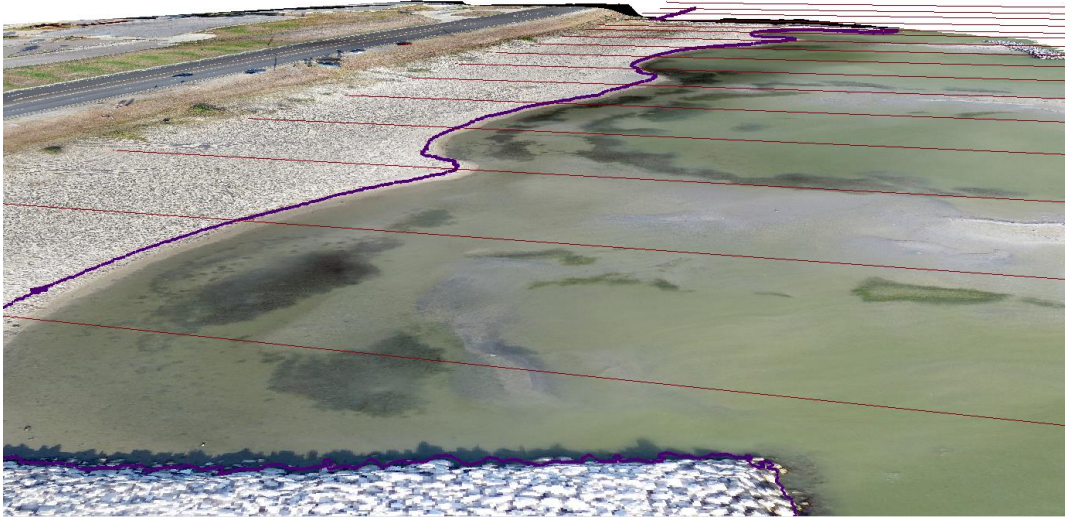
Figure 4.7: 3-dimensional model of August 24 – Radially filtered. The August 24 'Terrestrial' point set exhibited the highest accuracy (0.240 m (0.79 ft)) in MHHW contouring due to low flight altitude (90.53 m (297.0 ft) and low tide level (+ 13 cm NAVD88). Results shown in ArcScene.

Figure 4.8 and 4.9 show planimetric maps of the MHHW contour as rendered from August 24th radially

filtered point set and October 5th '*Denoised*' point set.
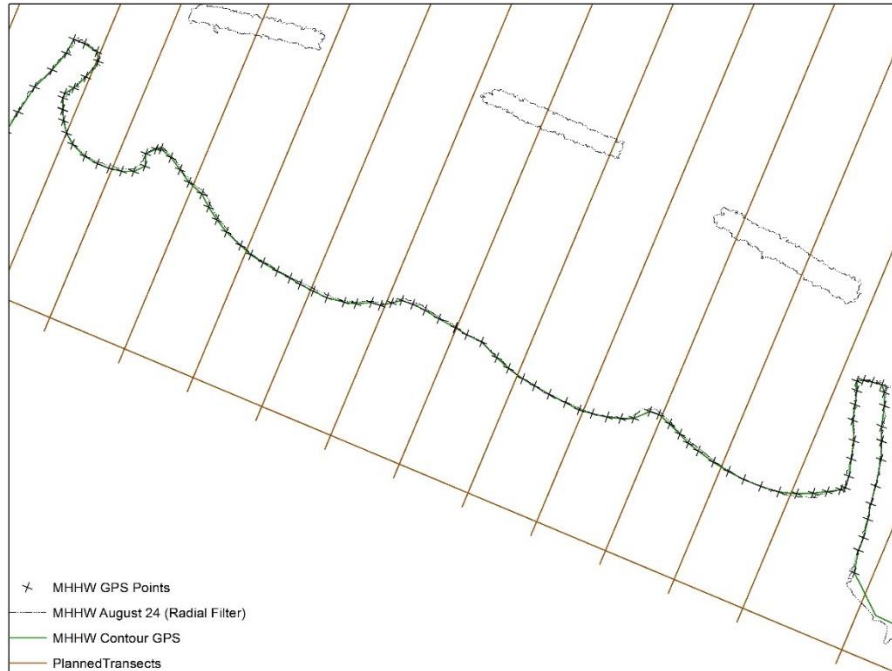
Figure 4.8: August 24 - Contour results from radially filtered 'Terrestrial' point cloud. The August 24th dataset exhibited the most accuracy in MHHW contour mapping.
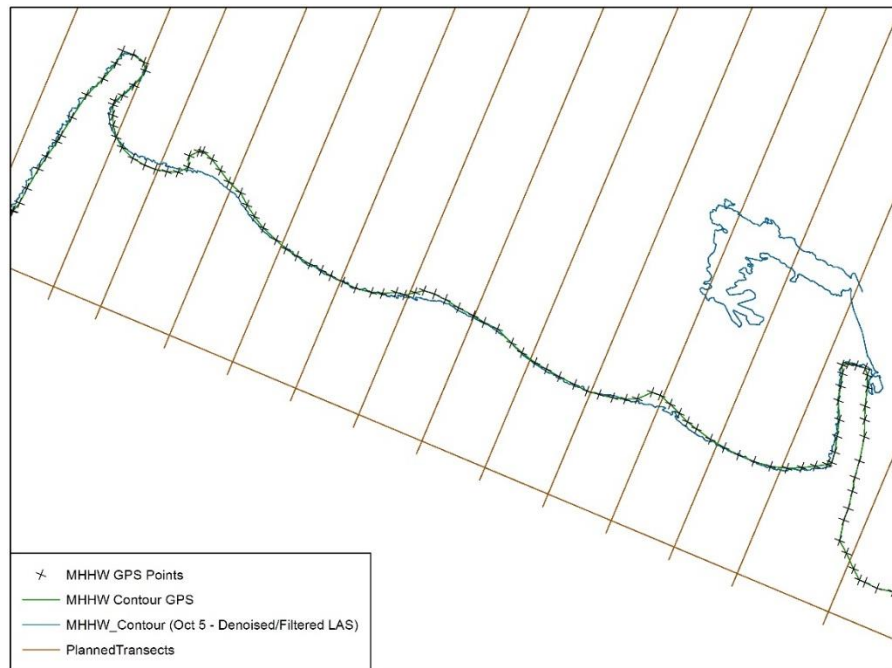
Figure 4.9: October 5 – Contour results from '*Denoised*' point cloud. Point cloud was filtered using LASnoise, LASheight, and classified with LASground. Addition research is needed to examine the potential for micro-scale coastal monitoring using UAS imagery and SfM processing.

Only one complete topographic RTK GPS survey was able to be completed from which all SfM data products were compared. A time gap of 44 days lapsed between the initial GPS survey on August 22, 2014 and the final eBee flight on October 5, 2014. Two cold front systems with winds up to 29 mph and 22 mph on September 13th and 25th respectively blew along Corpus Christi Bay between the August 22 GNSS survey and October 5, 2014 eBee flight. Despite these conditions, university beach has not required renourishment since the completion of construction in 2001 and is generally a low energy shoreline (Pers. Comm. Deidre Williams). The shoreline is protected from southeast winds by the land mass of Ward Island and the Encinal Peninsula. Breakwaters protect the beach from wave action driven by north winds. Though excessive change was not expected, shoreline position at the tidal interface may have changed significantly enough to shift the horizontal position of the MHHW contour during the 44 day time interval. It is not expected that any significant statistical deviation would be present in SfM point cloud comparisons. The vast majority of topographic GPS observations over water were on stable sea floor. Approximately, 37/814 GPS observations with water cover on October 5 (higher tide) were between the high waterline of October 5 and low waterline of August 24. These 37 comparisons were within the active high energy shoreline and may have been subject to minor morphological change. For this reason, it cannot be stated whether the higher and further landward MHHW contour positions reported from October 5 are artifacts of mismatched water surface locations due to turbid water and surface disturbance, or a correct representation of minute shoreline change since August 24.

4.6 Discussion

SfM through water is a very complex proposition. The entire workflow in both August 24th and October 5th flight scenarios are based on the correct matching of features with resolution < 3.6cm. Surface reflectance and wave interference will always play a role in coastal SfM datasets. The best solution for extracting 3-dimensional data along a turbid coastline is to find the depth of failure of a constrained (4 and 5-match minimum) dataset and employ a bathymetric inversion algorithm to seafloor bathymetry beyond this threshold.

All datasets except the October 5 unfiltered and October 5 radially filtered datasets have positive average residuals; joined SfM point cloud data was biased above actual seafloor surface. It is hypothesized that the positive average residual bias from 'clean' datasets is the result of SfM feature detector algorithms falsely identifying transient features such as glint and other radiometric anomalies on the water surface. The collected data suggests that the reason for the negative bias (-1.30 m (-4.26 ft)) for October 5 - radially filtered dataset was the extreme errors incurred during dense matching due to false image matching on the water surface. Although SfM may not be the ultimate solution in sub-surface aerial mapping, this research suggests that a combination of data and outputs from the SfM workflow may be pieced together in order to achieve better results underwater. The success in this research was the ability to map low-texture, low relief, sparsely vegetated shoreline and accurately place a MHHW contour in horizontal plane using 3-dimensional SfM point cloud and DEM. It is hypothesized that the optical inversion approach from low-altitude imagery may work using a sensor capable of recording multiple bands from the EM spectrum. Optical inversion by regression of reflectance values from smoothed RGB band ratios does show some significant correlation between reflectance and depth, although the depth of extinctions appears to be relatively shallow 0.5 m (~1.7 ft) - at least for low-altitude photography. Optical inversion did provide for complete coverage over water.

The impediment of water surface irregularities seemed to distort the correct calculation of 3-dimensional pixel locations. Introducing stringent match minimum constraints during the dense matching process severely restricted the extent of SfM bathymetry, having a negative impact on areal coverage. On the contrary, if the original unfiltered densified point cloud is processed with the presented filtering algorithm and classification techniques, coordinate locations from the seafloor can be found and areal coverage preserved. The correlation between increased residual of sub-surface GPS observations versus SfM z-values with increased water depth coverage suggests that SfM values sampled in this research may contain random noise. Figure 4.2 illustrates where SfM and GPS elevation correspondence deteriorates along a typical transect with relation to water level at time of survey. This correlation also indicates that z-values degraded with increased water depth as expected. A common pattern is observed for both flights

where correlation between SfM and GPS is relatively correspondent up to a depth of approximately 15 to 30 cm (0.5 ft to 1.0 ft). Figure 4.2 also shows the greater amplitude of noise seen in the October 5 SfM derivative elevation surface versus August 24. The difference in amplitudes of noise is attributed to the increased wind velocity as well as increased flying height for the October 5th mission. A combination of filtered point sets and ground classifying algorithms eliminated much of the noise, and functioned to properly map the true bottom.

UAS systems utilizing high resolution consumer grade digital cameras show great promise in the ability to provide suitable imagery for SfM mapping applications in coastal scenarios. The utility of SfM comes from the ability to process images from a non-metric camera in conjunction with inexpensive MEMS sensor input. This study provided an opportunity to assess the accuracy of UAS-SfM photogrammetry for mapping a low-energy littoral zone in Corpus Christi Bay, Texas. Results showed that accurate mapping can be accomplished along a low-texture, low relief, sparsely vegetated sandy shoreline. The radially filtered SfM point cloud matched within 6 cm of RTK GPS observation. The results also showed that a MHHW shoreline could be accurately located (+/- 0.24 m (0.79ft)) relative to GPS observation, demonstrating the potential of UAS for boundary surveying in coastal zones and hard to access regions. Impediment in deriving 3-dimensional data (and 2-dimensional vector derivatives) of the littoral zone stems from the failure of SfM algorithms when matching image features that contain the surface of turbid water; however, research suggests that SfM dense matching is possible along portions of the shoreline with shallow water cover (<0.304 m). The identification of the exact water clarity threshold was not determined. Band ratio optical inversion demonstrated that bathymetric information can be extracted from imagery obtained over turbid water in situations where light reflectance off the seafloor is minimal and feature detection is severely inhibited or prevented.

The best approach to generate a seamless topo-bathymetric DEM within the submerged zone coupled filtered SfM point cloud data with band ratio optical inversion along with integrated survey control. The seamless topo-bathymetric DEM produced in this research demonstrated that a complete 3-dimensional model can derived from UAS imagery and a network of RTK GPS observations. Although an extensive GNSS survey was used in this study for accuracy comparison and band ratio analysis for extraction of depth, future application of these methods for extraction of the seamless topo-bathy DEM should not require as many observations. It is hypothesized that proper quantity and application of targets might suffice for both final SfM model coordinate system transformation as well as for regression fitting

55

of band ratio optical inversion values to depths. Total hours spent on data acquisition would be kept to a minimum by implementing the least number of required GPS observations for quality assurance and targeting.

Accurate and inexpensive surveying of the littoral zone along the Texas coast has implications in land management, cadastral mapping, and erosion and habitat monitoring. UAS photogrammetry can provide a cost-effective and efficient method to obtain accurate elevation and spectral data at high spatial and temporal resolution. Traditional GPS surveys utilized for monitoring purposes are cost-prohibitive and require physically traversing the terrain with base and rover. The application of lidar and terrestrial scanning require significant cost investments in equipment and application. UAS-derived spatial data may provide a means to remotely survey areas where available budget cannot provide for intensive base and rover survey or laser scanning. For example, government agencies might implement a UAS-derived photogrammetry workflow that could produce a high volume, accurate elevation model at low cost for use in environmental monitoring, planning erosion response work, etc. UAS/SfM data could also be used to supplement other survey methods where accuracy of bathymetric SfM or optical inversion do not meet project specifications, but a high temporal frequency is desired (ex. monitoring applications). In Texas, SfM DEMs might be used for the delineation and quantification of artificial fill/buildup as part of the requirements for state-funded erosion protection programs (Texas Administrative Code 33.136).

In summary, results from this study suggest that dense and accurate 3-dimensional mapping of a littoral zone could be realized from imagery acquired with a low-cost consumer grade digital camera operated on an easy to fly, ultra-light UAS plus GPS observations used for quality assurance and targeting. The equivalent aerial survey comparison would be executed with manned aircraft equipped with a costly lidar system or via stereo photogrammetry employing a metric camera. It is apparent that the ease of acquisition and flexibility of UAS-based SfM photogrammetry represents a new paradigm in coastal mapping. As high resolution sensors and platforms continue to rapidly evolve, so too will the benefits and potential applications of the UAS/SfM approach.

FUTURE WORK

Remote sensing along the shoreline with UAS is in the infancy stage. Robust software packages incorporate high logic image processing techniques and complex algorithms that enable the UAS operator to produce high quality elevation data and orthophotos. Numerous challenges along the beach; however, remain unsolved. For example, SfM will fail where a surface of water exists because the same robust feature identification algorithms that enable automation impede or prohibit this process over water. The research does suggest that automated processes can be used along a littoral zone with some additional processing and the implementation of a patchwork of SfM products.

Future research is needed in order to compare SfM models across the beach surface and examining more rigorous effects of terrain variability on point measurements, such as by comparing to TLS. Full coverage becomes necessary for analysis because clusters of elevation samples must be more accurately analyzed along the shallow beach (<0.30 m water coverage) in order to identify exactly where image matching begins to deteriorate and alternative methods for deriving elevations becomes necessary. Turbidity/water clarity measurements may be a necessary component in decision making regarding the dissection of various elevation data for the purpose of shoreline mapping as this threshold is hypothesized to change with varying levels of turbidity.

Given the portability of modern UAS like the eBee and advances in meteorological forecasting such as tidal levels- a sufficient workflow could be to mobilize UAS operations during time of extreme low tide. If planning were carefully executed, low tide level as well as low wind and thus higher water clarity/less surface turbulence would be encountered allowing for more thorough image matching during SfM post-processing.

SfM efficiency around or through water might be increased with the use of a multi-band hyperspectral sensor from which imagery composed of only certain bands would be used in the SfM pipeline. According to Altena et al., most current SfM software suites transform imagery into grayscale, but the reflection of a specific type of substrate might be more in a certain band. Results from SfM

research along a shoreline in Belgium show a small benefit using the green band (Altena et al, 2014). Legleiter et al. (2011) have success using particular color bands from an Airborne Imaging Spectrometer for Applications which records data from 63 spectral bands between 401 and 982 nm.

Bathymetric optical inversion could be improved by utilizing a near infrared (NIR) sensor. Reflectance values in the NIR band could be used to effectively normalize other bands' reflectance over water (Figure 6.0). The band ratio method implemented in this research albeit regression was driven by an extensive network of GPS observations instead of a sparse network. A sparse network of GNSS control might enable a dataset recorded using a NIR sensor to be more accurately used in optical inversion resulting in the extraction of more accurate depth information with less hours and equipment time spent.

Another area of future work is the assessment of the accuracy of contouring a line interpolated from the optical inversion DEM. This becomes important when tidal levels reach above a threshold where another dataset may be present and data derived from optical inversion must be clipped at a particular contour. The accuracy of other water level contours would be an important assessment of the quality of optical inversion DEM. For example, if imagery is captured at a moment of tidal levels at MHHW, can a suitable contour be interpolated at mean sea level? Can the SfM point cloud be accurately clipped using this information in order to use more accurate shallow water point cloud data in lieu of optical inversion DEM? A simulation method would provide more accurate data on the proper methods for the merging of Sfm datasets and optical inversion rasters.

Figure 6.1: Example of potential NIR sensor for use with UAS. Tetracam's Agricultural Digital Camera (ADC) contains a sensor capable of recording Red, Green, and NIR (Tetracam, 2015).

Another source of the error found along the terrestrial point sets for both flights were the effect of shoreline vegetation. One drawback of SfM point clouds versus TLS is the incorporation of vegetative canopies in the final point set. Additional research is needed in the area of littoral boundary surveying and the removal or filtering of surface returns that include flat vegetation of a relatively homogenous height that is typical of littoral areas along the Gulf of Mexico. Successful aerial mapping of the coast line and production of accurate DEMs will require the filtering out of species such as smooth cordgrass (*Spartina alterniflora)*, black mangrove (*Avicennia germinans*) and other typical marsh species (i.e. *Spartina spp.)*. RapidLasso has some ground point filters that were used in this research, but were not implemented for terrestrial points. The bulk majority of the beach was unvegetated where little residual was seen.

Another area of potential research is the use of light filters or lens polarization in order to perform post-processing on photographs with specific properties (Figure 6.1). A linear polarizing filter correctly placed in front of the camera lens might be able to effectively suppress glare and reflection from the water surface by filtering out scattered unorganized light (Matsuyama et al, 2004).

Figure 6.2: Polarizing light before it enters the lens during image acquisition may facilitate better SfM results through water.

SfM processing along a littoral zone is not a straight forward process. Success will depend on flight planning accordingly to meteorological/marine conditions so that ideal radiometric qualities are obtained in the initial imagery. This thesis has identified and quantified inherent areas of weakness of processing UAS imagery with SfM along the littoral zone, and proposed methods to utilize the same imagery in areas where SfM fails.

<center>**REFERENCES**</center>

Altena, B., Cockx, L., Goedemé, T. 2014. A proxy for variance in dense matching over homogeneous terrain. Faculty of Industrial Engineering, KU Leuven, Sint-Katelijne-Waver, Belgium

Beraldin, J.-A., 2004. Integration of Laser Scanning and Close-Range Photogrammetry - The Last Decade and Beyond. XXth International Society for Photogrammetry and Remote Sensing Congress, Commission VII, Istanbul, Turkey, pp. 972-983.

Boehler, W., and Marbs, A., 2004. 3D scanning and photogrammetry for heritage recording: a comparison. Proceedings of the 12th International Conference on Geoinformatics, University of Gavle, Sweden, pp. 291–298.

Draeyer, B. and Strecha, C. 2014. White paper: How accurate are UAV surveying methods? February 2014.

Federal Aviation Administration (FAA). 2015. https://www.faa.gov/uas/civil_operations/ Accessed April 23, 2015.

Fonstad, M.A., Dietrich, J.T., Courville, B.C., Jensen, J.L., and Carbonneau, P.E. 2012. Topographic structure from motion: a new development in photogrammetric measurement. Earth Surface Processes and Landforms 38, 421-430 (2013).

Fu, Yi-Ge., Zhou, J., and Deng, L. 2014. Surveillance of a 2d plane area with 3d deployed cameras. Sensors 14(2), 1988-2011; DOI:10.3390/s140201988-Article. Department of Automation, Tsinghua University, Beijing 100084, China

Furukawa, Y. and Ponce, J. 2010. Accurate, Dense, and Robust Multi-View Stereopsis. IEEE Transactions on Pattern Analysis and Machine Intelligence, Vol. 32, Issue 8, Pages 1362-1376, August 2010

General Bathymetric Chart of the Ocean (GEBCO). 2014. The IHO-IOC GEBCO Cook Book. IHO Publication B-11, IOC Manuals and Guides, 63. September 2014

Graham, P.R. 2005. Determination of Structure from Motion using aerial imagery. Thesis for M.S. Department of Electrical and Computer Engineering, Air Force Institute of Technology.

Harris, C., and Stephens, M. A combined corner and edge detector. In Procedings of the Alvey conference. Pages 189-192. 1988.

Isenburg, M. (2014). Removal of Cloud Returns with a Coarse DTM. Posted on September 16, 2014 by Martin Isenburg http://rapidlasso.com/category/tutorials/

Jebara, T., Azarbayejani, A., and Pentland, A. 2001. 3D Structure from 2D Motion. MIT Media Laboratory. ftp whitechapel.media.mit.edu /pub/sfm

Jiang, Q., Zeng, Y., Liu, Q., Jing, H. 2012. Attitude and Heading Reference System for Quadrotor Based on MEMS Sensors. 2012 Second International Conference on Instrumentation & Measurement, Computer, Communication and Control

Johnson, K., Nissen, E., Saripalli, S., Arrowsmith, J.R., McGarey, P., Scharer, K., Williams, P., and Blisniuk, K. 2014. Rapid mapping of ultrafine fault zone topography with structure from motion. Geosphere; October 2014; v. 10; no. 5; p. 969–986; DOI:10.1130/GES01017.1

Matsuyama, T., Ishiyama, T., and Omura, Y. 2004. Nikon projection lens update, Proc. SPIE 5377, Optical Microlithography XVII, 730 (May 28, 2004); DOI:10.1117/12.537206; http://dx.doi.org/10.1117/12.537206

Kelcey, J.and Lucieer, A.2012. Sensor Correction of a 6-Band Multispectral Imaging Sensor for UAV Remote Sensing. Remote Sens. 2012, 4, 1462-1493; DOI:10.3390/rs4051462. ISSN 2072-4292. www.mdpi.com/journal/remotesensing

Legleiter, C. J., P. J. Kinzel, and B. T. Overstreet (2011), Evaluating the potential for remote bathymetric mapping of a turbid, sand-bed river: 2. Application to hyperspectral image data from the Platte River, Water Resour. Res., 47, W09532, DOI:10.1029/2011WR010592.

Lucieer, A., de Jong, S.M., Turner, D. 2014. Mapping landslide displacements using Structure from Motion (SfM) and image correlation of multi-temporal UAV photography. Progress in Physical Geography 2014, Vol. 38(1) 97–116. DOI: 10.1177/0309133313515293

Linder, W. 2009. Digital Photogrammetry: a Practical Course, third edition. Springer-Verlag Berlin Heidelberg.

Ma, D., Shiau, J., Wang, I. and Lin, Y. 2012. Attitude determination using a MEMS-based flight information measurement unit. Sensors 2012, 12, 1-23; DOI:10.3390/s120100001

McFarland, J. 2013. House Bill 325 to Amend Open Beaches Act. http://www.oilandgaslawyerblog.com/2013/04/house-bill-325-to-amend-open-b.html Accessed 20 October 2014.

Megyesi, Z. 2009. Dense Matching Methods for 3D Scene Reconstruction from Wide Baseline Images. Ph.D. Dissertation. E¨otv¨os Lor´and University, Budapest, Hungary.

National Oceanic and Atmospheric Administration (NOAA). 2003. Computational techniques for tidal datums handbook. NOAA Special Publication NOS CO-OPS 2. Silver Spring, Maryland. September 2003.

National Oceanic and Atmospheric Administration (NOAA). 2015. Tidal Datums. http://tidesandcurrents.noaa.gov/datum_options.html Accessed May 3, 2015.

Pan, Z., Fernandez-Diaz, J.C., Glennie, C.L., Starek, M. 2014. Comparison of Bathymetry and Seagrass Mapping with Hyperspectral Imagery and Airborne Bathymetric LiDAR in a Shallow Estuarine Environment. Journal of Selected Topics in Applied Earth Observations and Remote Sensing, Vol 8.

Pix4D Website. 2015. Various site pages: https://support.pix4d.com/hc/en-us/articles/202557409-Step-1-Before-Starting-a-Project-1-Designing-the-Images-Acquisition-Plan

Dall'Asta, E. and Roncella, R. 2014. A comparison of semiglobal and local dense matching algorithms for surface reconstruction. The International Archives of the Photogrammetry, Remote Sensing and Spatial Information Sciences, Volume XL-5, 2014 ISPRS Technical Commission V Symposium, 23 – 25 June 2014, Riva del Garda, Italy

Schubert, J.E., Gallien, T.W., Majd, M.S., and Sanders, B.F. 2015. Terrestrial laser scanning of anthropogenic beach berm erosion and overtopping. Journal of Coastal Research, V31,1 47–60

Sensefly. 2014. eBee: An Extended User's Manual. Sensefly, a Parrot Company.

Skarlatos, D. and Kiparissi, S. 2012. Comparison of laser scanning, photogrammetry and sfm-mvs pipeline applied in structures and artificial surfaces. ISPRS Annals of the Photogrammetry, Remote Sensing and Spatial Information Sciences, Volume I-3, 2012

Snavely, K.N. 2008. Scene Reconstruction and Visualization from Internet Photo Collections, Thesis (Phd). Computer Science and Engineering, University of Washington.

Snavely, N., Seitz, S.M., and Szeliski, R. 2006. Photo Tourism: Exploring image collections in 3D. ACM Transactions on Graphics (Proceedings of SIGGRAPH 2006), 2006.

Snavely, N., Simon, I., Goesele, M., Szeliski, R., and Seitz, S.M. 2010. Scene Reconstruction and Visualization From Community Photo Collections. Proceedings of the IEEE | Vol. 98, No. 8, August 2010

Strecha, C., (2014). Pix4D – Error Estimation. February 10, 2014. Pix4D Online Support. https://support.pix4d.com/hc/en-us/articles/202559149-How-does-Pix4D-estimate-the-error-from-Tie-points-

Teeravech, K. 2015. Generating Orthophotos using SfM technique. PowerPoint presentation. Remote Sensing and Geographic Information Systems, School of Engineering and Technology, AIT. Thailand.

Tetracam. 2015. http://www.tetracam.com/pdf/ADC_Brochure_Replacement.pdf Accessed April 22, 2015.

Tola E., Lepetit V., and Fua P. Daisy, 2010. An Efficient Dense Descriptor Applied to Wide Baseline Stereo. IEEE Transactions on Pattern Analysis and Machine Intelligence, 32(5):815– 830.

Vallet, J., Panissod, F., Strecha, C., Tracol, M. 2011. Photogrammetric performance of an ultra light weight swinglet "UAV"

Vasuki, Y., Holden, E. Kovesi, P. and Micklethwaite, S. 2014. Semi-automatic mapping of geological Structures using UAV-based photogrammetric data: An image analysis approach. Computers & Geosciences 69 (2014) 22–32.

United States Government Accountability Office (USGOA). 2013. UNMANNED AIRCRAFT SYSTEMS Continued Coordination, Operational Data, and Performance Standards Needed to Guide Research and Development. Statement of Gerald L. Dillingham, Ph.D. Director, Physical Infrastructure Issues

United States Army Corps of Engineers. 2013. Hydrographic Surveying, Engineer Manual. 30 November 2013.

Westaway, R.M., Lane, S.N., Hicks, D.M. 2001. Remote sensing of clear-water, shallow, gravel-bed rivers using digital photogrammetry. Photogrammetric Engineering & Remote Sensing, November 2001.

Williams, D., 2002. A Recreational Beach Fill for Texas A&M University-Corpus Christi: Coastal Processes and Functional Design, Thesis (M.S), Texas A&M Corpus Christi, TX., 249 p.http://www.cbi.tamucc.edu/CHRGIS/University-Beach/

Williams, D., 2005. Monitoring, analysis and interpretation of the post-construction evolution of a restored beach at TAMU-CC. Final report submitted to Texas General Land Office – Coastal Management Program. January 10, 2005

Wohlfeila, J., Strackenbrockb, B. and Kossyk, I. 2013. Automated high resolution 3d reconstruction of cultural heritage using multi-scale sensor systems and semi-global matching. The International Archives of the Photogrammetry, Remote Sensing and Spatial Information Sciences, Volume XL-4/W4, 2013 ISPRS Acquisition and Modelling of Indoor and Enclosed Environments 2013, 11 – 13 December 2013, Cape Town, South Africa

Wolf, P., DeWitt, B., and Wilkinson, B. 2014. Elements of Photogrammetry with Application in GIS, Fourth Edition

Woodget, A.S., Carbonneau, P.E., Visser, F., Maddock, I., and Habit, E. 2014. Quantifying fluvial topography using UAS imagery and SfM-photogrammetry. University of Worcester.

Wu, C. 2015. VisualSFM : A Visual Structure from Motion system. http://ccwu.me/vsfm/doc.html#size

APPENDICES

Appendix A: Average depth of water cover where survey-grade accuracy was achieved sub-surface.

Average Depth of Water Cover Overall (residual error < 0.03 m/0.2 ft)

	No. Pnts	**Average (ft)**	**(m)**
August 24 - Radially filtered	**7,547,058**	Overall: 0.54	0.165
		Residual<0.03 m	
Sub-surface-clip	**261**	0.14	0.043
Sub-surface	**222**	0.15	0.046
October 5 - Radially filtered	**4,232,744**	Overall: 1.83	0.558
		Residual<0.03 m	
Sub-surface-clip	**516**	0.77	0.235
Sub-surface	**449**	0.92	0.280
October 5 - 'Denoised'	**5,237,184**	1.54	0.469
Sub-surface	**393**	1.04	0.317
October 5 - 4 match point	**3,230,080**	Overall: 1.33	0.405
		Residual<0.03 m	
Sub-surface-clip	**268**	1.06	0.323
Sub-surface	**216**	1.16	0.354
October 5 - 5 match point	**2,988,999**	Overall: 1.21	0.370
		Residual<0.03 m	
Sub-surface-clip	**222**	1.00	0.305
Sub-surface	**180**	1.62	0.494

Appendix B: Analysis of SfM using RTK GPS survey as control.

August 24: - University Beach, 80 calibrated images

Altitude: 90.53m (297ft)

Wind: southeast 7 knots

Georeferencing: 6 GCPs (6 3D), mean error = 1.9 cm (0.062 ft)

Ground Sampling Distance: 2.92 cm

Average water level shot (9 GPS observations) at time of flight: 13.6 cm (0.446 ft) NAVD88

August 24: - Unfiltered LAS Dataset

Number of point records:	**8,542,778**

Point density: 65.44 per m^2 (6.08 per ft^2)

Point spacing: 12.50 cm (0.41 ft)

Zmin: 3.225 m (-10.581 ft)

Zmax: 21.590 m (70.833 ft)

August 24: - Densified Radially Filtered (10XGSD) LAS Dataset[A24-F]

Number of point records:	**7,547,058**

Point density: 58.66 per m^2 (5.45 per ft^2)

Point spacing: 13.1cm (0.43ft)

Zmin: -3.10 m (-10.17 ft)

Zmax: 21.51 m (70.56 ft)

Terrestrial Joined[A24-F]

	(ft)	(m)
Total Joined Points		**644**
Average **residual**	0.18	0.056
Std Dev	0.51	0.155
Squared Sum	188.36	57.411
RMSE	0.54	0.165

Sub-surface – Clipped Joined[A24-F]

	(ft)	(m)
Total Joined Points		**261**
Average residual	0.50	0.151
Std Dev	1.15	0.350
Squared Sum	408.76	124.591
RMSE	1.25	0.381
Lower 95%(2σ Residuals)	-1.80	-0.550
Upper 95%(2σ Residuals)	2.79	0.852
Std Dev(Abs(residual))	1.15	0.350

Water Depth Analysis

	(ft)	(m)
Avg. Water Depth	0.54	0.165

Average Water Depth (Classified by σ)

	(ft)	(m)
Residuals<1σ	0.29	0.089
1σ>Residuals>2σ	1.19	0.364
2σ>Residuals>3σ	3.05	0.929
Residuals>3σ	3.40	1.036
Avg Water Depth where residual <0.2' (0.03m)	0.14	0.041

Sub-Surface Joined[A24-F]

Total Joined Points		**222**
	(ft)	**(m)**
Average residual	0.18	0.056
Std Dev	0.93	0.282
Squared Sum	197.71	60.262
RMSE	0.94	0.288
Average	0.18	0.055
Lower 95%(3σ Residuals)	-1.67	-0.509
Upper 95%(3σ Residuals)	2.03	0.619
Std Dev(Abs(residual))	0.93	0.283

Water Depth Analysis

Avg. Water Depth	0.36	0.110

Average Water Depth (Classified by σ)

	(ft)	**(m)**
Residuals<1σ	0.22	0.069
1σ>Residuals>2σ	0.99	0.301
2σ>Residuals>3σ	1.37	0.417
Residuals>3σ	1.87	0.570
Avg Water Depth where residual <0.2ft (0.03m)	0.15	0.050

October 5: – University Beach, 331 Calibrated images

October 5, 2014: four comparisons are made. First point set is filtered using standard Pix4D moving window (10XGSD). Second point set is filtered using a reference surface and LAStools (LASheight, LASnoise, LASground). Two alternate processing methods are shown, 4-match minimum and 5-match minimum dense matching.

Altitude: 115.52m (379ft)

Wind: 10 knots, 157 degrees.

Georeferencing: 16 GCPs (16 3D), mean error = 2.7 cm (0.088 ft) (Quality Report)
Average Ground Sampling Distance: 3.56 cm

Average water level shot (3 shots) at time of flight: 0.439m (1.442 ft) NAVD88

October 5: – Densified Unfiltered LAS Pointset

Number of point records:	**5,662,517**

Point density: 75.78 per m^2 (7.04 per sq ft)

Point spacing: (0.38 ft)

Zmin: 21.437 m (-70.33 ft)

ZMax: 10.339m (33.92 ft)

October 5, Densified Radially Filtered LAS Pointset: (Pix4D Filtered)[O5-F]

Total Points: **4,232,744**

Point density: 57.800 m^2 5.37 (per ft^2)

Point spacing: 13.1 cm (0.43 ft)

Zmin: 21.071 m (-69.13 ft)

ZMax: 10.168 m (33.36 ft)

Terrestrial Joined[O5-F]

Total Joined Points		**518**
	(ft)	**(m)**
Average residual	0.29	0.089
Std Dev	0.64	0.195
Squared Sum	256.97	78.326
RMSE	0.70	0.215

Sub-Surface – Clipped Joined[O5-F]

Total Joined Points		**516**
	(ft)	**(m)**
Average residual	-1.59	-0.484
Std Dev	11.97	3.650
Squared Sum	75280.36	22945.734
RMSE	12.08	3.682
Average	-1.56	-0.476
Lower 95%(3σ Residuals)	-25.28	-7.707
Upper 95%(3σ Residuals)	22.16	6.754
Std Dev(Abs(residual))	11.86	3.615

Water Depth Analysis

Avg. Water Depth	1.83	0.559

Average Water Depth (Classified by σ)

	(ft)	**(m)**
Residuals<1σ	1.67	0.508
1σ>Residuals>2σ	2.88	0.877
2σ>Residuals>3σ	2.35	0.715
Residuals>3σ	3.28	0.998
Avg Water Depth where residual <0.2' (0.03m)	0.77	0.234

Sub-Surface Joined[O5-F]

Total Joined Points	**449**

	(ft)	(m)
Average residual	-4.26	-1.299
Std Dev	11.64	3.548
Squared Sum	69008.42	21034.022
RMSE	12.40	3.779
Average	-4.26	-1.299
Lower 95%(3σ Residuals)	-27.55	-8.391
Upper 95%(3σ Residuals)	19.02	5.794
Std Dev(Abs(residual))	11.64	3.546

Water Depth Analysis

	(ft)	(m)
Avg. Water Depth	1.77	0.540

Average Water Depth (Classified by σ)

	(ft)	(m)
Residuals<1σ	1.69	0.516
1σ>Residuals>2σ	1.78	0.542
2σ>Residuals>3σ	2.35	0.715
Residuals>3σ	3.28	0.998
Avg Water Depth where residual <0.2' (0.03m)	0.92	0.279

October 5: – '*Denoised*' (LAStools)[O5-DE]

Number of point records:		**5,237,184**

Point density: 77.82 m 7.23 (per ft^2)

Point spacing: 11.3 cm (0.37 ft)

Zmin: 2.335 m (-7.66 ft)

Zmax: 9.062 m (29.73 ft)

Final filtering and processing (see page XX for details)

Terrestrial Joined[O5-DE]

Total Joined Points		**538**
	(ft)	**(m)**
Average **residual**	0.30	0.101
Std Dev	0.66	0.220
Squared Sum	283.79	94.596
RMSE	0.73	0.242

Sub-surface Clip [O5-DE]

Omitted, filtered out above surface points in filter process.

Sub-surface ('*Denoised*') Joined[O5-DE]

	(ft)	(m)
Total Joined Points		**393**
	(ft)	**(m)**
Average Residual	0.96	0.292
Std Deviation	1.61	0.489
Squared Sum	1373.54	418.660
RMSE	1.87	0.570
Lower 95%(Residuals)	-2.25	-0.687
Upper 95%(Residuals)	4.17	1.271
Std Dev(Abs(residual))	1.34	0.409

Water Depth Analysis

	(ft)	(m)
Avg. Water Depth	1.54	0.468

Average Water Depth (Classified by σ)

	(ft)	**(m)**
Residuals<1σ	1.08	0.328
1σ>Residuals>2σ	1.60	0.487
2σ>Residuals>3σ	2.95	0.900
Residuals>3σ	4.80	1.463
Ave Water Depth where residual <0.2' (0.03m)	1.04	0.316

Alternate Processing1 (4-match minimum point cloud densification)[O5-AP1]

Number of point records:	**3,230,080**

Point density: 52.63 per m^2 (4.89 per ft^2)
Point spacing: 13.72 cm (0.45 ft)
Zmin: -3.395 m (-11.14 ft)
Zmax: 9.980 m (32.74 ft)

Terrestrial Joined [O5-AP1]

Total Joined Points		**537**
	(ft)	**(m)**
Average	0.23	0.071
Std Dev	0.65	0.199
Squared Sum	256.97	78.324
RMSE	0.69	0.211

Sub-surface – Clipped Joined [O5-AP1]

Total Joined Points		**268**
	(ft)	**(m)**
Average Residual	0.65	0.198
Std Deviation	1.42	0.432
Squared Sum	652.96	199.023

	(ft)	(m)
RMSE	1.56	0.476
Lower 95%(Residuals)	-2.19	-0.667
Upper 95%(Residuals)	3.49	1.063
Std Dev(Abs(residual))	1.21	0.368

Water Depth Analysis

	(ft)	(m)
Avg. Water Depth	1.33	0.405
AvgWaterDepth	**(ft)**	**(m)**
Residuals<1σ	1.07	0.325
1σ>Residuals>2σ	1.84	0.560
2σ>Residuals>3σ	2.63	0.800
Residuals>3σ	3.94	1.201
Ave Water Depth where residual <0.2' (0.03m)	1.06	0.323

Sub-Surface Joined [O5-AP1]

	(ft)	(m)
Total Joined Points		**216**
	(ft)	**(m)**
Average Residual	0.31	0.094
Std Deviation	0.94	0.288
Squared Sum	213.47	65.065
RMSE	0.99	0.303
Lower 95%(Residuals)	-1.58	-0.482
Upper 95%(Residuals)	2.20	0.670
Std Dev(Abs(residual))	0.72	0.220

Water Depth Analysis [O5-AP1]

	(ft)	(m)
Avg. Water Depth	1.36	0.415
AvgWaterDepth	**(ft)**	**(m)**
Residuals<1σ	1.15	0.349
1σ>Residuals>2σ	1.31	0.400
2σ>Residuals>3σ	1.87	0.571
Residuals>3σ	3.47	1.056
Ave Water Depth where residual <0.2' (0.03m)	1.16	0.354

October 5, – Alternate Processing2 (5-match minimum point cloud densification) [O5-AP2]

Number of point records:	**2,988,999**

Point density: 50.91 per m^2 (4.73 per ft^2)
Point spacing: 14.02 cm (0.46 ft)
Zmin: -2.231 m (-7.32 ft)
Zmax: 9.412 m (30.88 ft)

Terrestrial Joined[O5-AP2]

Total Joined Points		537
	(ft)	**(m)**
Average	0.23	0.069
Std Dev	0.65	0.200
Squared Sum	259.50	86.500
RMSE	0.70	0.232

Sub-surface – Clipped Joined [O5-AP2]

Total Joined Points		222
	(ft)	**(m)**
Average Residual	0.53	0.163
Std Deviation	1.27	0.389
Squared Sum	424.25	129.313
RMSE	1.38	0.421
Lower 95%(Residuals)	-2.01	-0.614
Upper 95%(Residuals)	3.08	0.940
Std Dev(Abs(residual))	1.05	0.319

Water Depth Analysis

Avg. Water Depth	1.21	0.370
AvgWaterDepth	**(ft)**	**(m)**
Residuals<1σ	0.99	0.301
1σ>Residuals>2σ	1.52	0.462
2σ>Residuals>3σ	2.16	0.657
Residuals>3σ	3.14	0.957
Ave Water Depth		
where residual <0.2' (0.03m)	1.00	0.305

Sub-Surface Joined[O5-AP2]

Total Joined Points		180
	(ft)	**(m)**
Average Residual	0.31	0.094
Std Deviation	0.92	0.282
Squared Sum	170.64	52.012
RMSE	0.97	0.297

	(ft)	(m)
Lower 95%(Residuals)	-1.54	-0.470
Upper 95%(Residuals)	2.15	0.657
Std Dev(Abs(residual))	0.68	0.208

Water Depth Analysis

Avg. Water Depth	1.33	0.404
	(ft)	**(m)**
Residuals<1σ	1.11	0.338
1σ>Residuals>2σ	1.20	0.367
2σ>Residuals>3σ	2.17	0.660
Residuals>3σ	3.41	1.039
Avg Water Depth where residual <0.2' (0.03m)	1.62	0.493

Optical Inversion - Red band normalized ln(Blue)/ln(Green)

	(ft)	(m)
Total Joined Points		**728**
	(ft)	**(m)**
Average Residual	0.00	-0.001
Std Deviation	1.16	0.354
Squared Sum	981.80	299.257
RMSE	1.16	0.354
Lower 95%(Residuals)	-2.33	-0.709
Upper 95%(Residuals)	2.32	0.707
Std Dev(Abs(residual))	0.75	0.230

Water Depth Analysis

Avg. Water Depth	1.53	0.466
Average Water Depth (Classified by σ)		
	(ft)	**(m)**
Residuals<1σ	1.11	0.338
1σ>Residuals>2σ	1.94	0.592
2σ>Residuals>3σ	4.71	1.436
Residuals>3σ	none	none
Avg. Water Depth where residual <0.2' (0.03m)	1.32	0.403

October 5 - : Hybrid Model

Total Joined Points		**1360**

	(ft)	(m)
Average Residual	0.18	0.054
Std Deviation	1.04	0.316
Squared Sum	1504.51	458.579
RMSE	1.05	0.321
Lower 95%(Residuals)	-1.89	-0.577
Upper 95%(Residuals)	2.25	0.686
Std Dev(Abs(residual))	0.75	0.229

Appendix C: MHHW contour analysis – in-situ GPS observations versus SfM MHHW contour interpolated from point cloud TIN.

August 24 - (Radially Filtered)

MHHW Analysis - Residuals by Near Table

Negative Values are seaward of MHHW Control Line

	(ft)	(m)
Average Residual	-0.79	-0.240
Std Deviation	1.58	0.483
Squared Sum	397.13	121.046
RMSE	1.77	0.539

October 5 - (*Denoised*)

MHHW Analysis - Residuals by Near Table

Negative Values are seaward of MHHW Control Line

	(ft)	(m)
Average Residual	1.69	0.515
Std Deviation	6.16	1.879
Squared Sum	4370.64	1332.187
RMSE	6.39	1.948

October 5 - (Alternate Processing - 4-match minimum)

MHHW Analysis - Residuals by Near Table

Negative Values are seaward of MHHW Control Line

	(ft)	(m)
Average Residual	1.46	0.446
Std Deviation	6.30	1.919
Squared Sum	4803.57	1464.147
RMSE	6.46	1.970

October 5 - (Alternate Processing2 - 5-match minimum)

MHHW Analysis - Residuals by Near
Table

Negative Values are seaward of MHHW Control Line

	(ft)	(m)
Average Residual	1.84	0.561
Std Deviation	6.10	1.860
Squared Sum	4672.84	1424.299
RMSE	6.37	1.943

DEM Combo - Optical Inversion (August 24), October 5 (*denoised*),
October 5 (terrestrial point cloud)

MHHW Analysis - Residuals by Near
Table

Negative Values are seaward of MHHW Control Line

	(ft)	(m)
Average Residual	2.09	0.636
Std Deviation	6.37	1.940
Squared Sum	5206.11	1586.843
RMSE	6.70	2.042